Evaluation of Multiorbital SAR and Multisensor Optical Data for Empirical Estimation of Rapeseed Biophysical Parameters

Aubin Allies, Antoine Roumiguié, Jean-François Dejoux, Rémy Fieuzal, Anne Jacquin, Amanda Veloso, Luc Champolivier, and Frédéric Baup

***Abstract*—This article aims to evaluate the potential of multitemporal and multiorbital remote sensing data acquired both in the microwave and optical domain to derive rapeseed biophysical parameters (crop height, dry mass, fresh mass, and plant water content). Dense temporal series of 98 Landsat-8 and Sentinel-2 images were used to derive normalized difference vegetation index (NDVI), green fraction cover (fCover), and green area index (GAI), while backscattering coefficients and radar vegetation index (RVI) were obtained from 231 mages acquired by synthetic aperture radar (SAR) onboard Sentinel-1 platform. Temporal signatures of these remote sensing indicators (RSI) were physically interpreted, compared with each other to ground measurements of biophysical parameters acquired over 14 winter rapeseed fields throughout the 2017–2018 crop season. We introduced new indicators based on the cumulative sum of each RSI that showed a significant improvement in their predictive power. Results particularly reveal the complementarity of SAR and optical data for rapeseed crop monitoring throughout its phenological cycle. They highlight the potential of the newly introduced indicator based on the VH polarized backscatter coefficient to estimate height ($R^2 = 0.87$), plant water content ($R^2 = 0.77$, from flowering to harvest), and fresh mass ($R^2 = 0.73$) and RVI to estimate dry mass ($R^2 = 0.82$). Results also demonstrate that multiorbital SAR data can be merged without significantly degrading the performance of SAR-based relationships while strongly increasing the temporal sampling of the monitoring. These results are promising in view of assimilating optical and SAR data into crop models for finer rapeseed monitoring.**

Manuscript received April 15, 2021; revised June 13, 2021 and June 17, 2021; accepted June 27, 2021. Date of publication July 8, 2021; date of current version July 29, 2021. This work was supported by the Institut Europlace de Finance, Pacifica and the foundation Grameen Crédit Agricole in the framework of the "Initiative de Recherche—Risques et protection financière de l'agriculture" Fonds d'Action Stratégique des Oléoprotéagineux in the framework of the "Colza Digital" project. *(Corresponding author: Aubin Allies.)*

Aubin Allies is with the Institut Europlace de Finance, 75002 Paris, France with the Airbus Defence and Space Geo, 31030 Toulouse, France, and also with the Centre d'Etudes Spatiales de la Biosphère, UMR 5126 UPS-CNES-CNRS-IRD-INRAE, 31400 Toulouse, France (e-mail: allies.aubin@orange.fr).

Antoine Roumiguié, Anne Jacquin, and Amanda Veloso are with the Airbus Defence and Space Geo, 31030 Toulouse, France (e-mail: antoine.roumiguie@airbus.com; anne.jacquin@airbus.com; amanda.veloso@airbus.com).

Jean-François Dejoux, Rémy Fieuzal, and Frédéric Baup are with the Centre d'Etudes Spatiales de la Biosphère, UMR 5126 UPS-CNES-CNRS-IRD-INRAE, 31400 Toulouse, France (e-mail: jean-francois.dejoux@cesbio.cnes.fr; remy.fieuzal@cesbio.cnes.fr; frederic.baup@cesbio.cnes.fr).

Luc Champolivier is with the Station Inter-Instituts, Terres Inovia, 31450 Baziège, France (e-mail: l.champolivier@terresinovia.fr).

Digital Object Identifier 10.1109/JSTARS.2021.3095537

***Index Terms*—Biomass, crop height, crop monitoring, Landsat-8, plant water content, rapeseed, Sentinel-1, Sentinel-2.**

I. Introduction

In THE context of global change and an increasing world demography, one of the major issues for mankind is to develop agriculture practices allowing to ensure together food security, sustainability of natural resources, and economic profitability for farmers [1], [2]. To address these challenges, precision agriculture became an essential scientific topic [3]. Precise crop monitoring systems generally rely on the high-frequency acquisition and assessment of crop biophysical parameters (BP) such as green/leaf area index (GAI/LAI), dry (DM) and fresh masses (FM), crop height, or plant water content (PWC). These parameters are key variables since they express the phenological and physiological plant response to meteorological events [4], [5], pest and diseases outbreaks [6], fertilizer applications [7], or water management practices [8]. They are, in addition, paramount for crop yields estimation from modeling approaches [9], [10]. However, for most crops, *in situ* ground measurements are lacking. Ground survey of such parameters is time-consuming and, thus, cannot be reproduced at a fine spatio-temporal scale in real or near-real time. To overcome this limitation, satellite remote sensing has been recognized as an effective solution to monitor spatio-temporal evolutions of crops at scales compatible with decision makers of landscape management [11], [12].

Both optical and microwave domains have been intensively explored for crop parameters retrieval [13]–[15]. In the optical domain, a large panel of studies has demonstrated the interest in using reflectance or vegetation index to derive BP, in particular, LAI [16]–[18], biomass [19], or crop height [20]. However, the use of optical data has major drawbacks, first and foremost, their sensitivity to weather and lightning conditions that can drastically limit their availability in terms of temporal frequency. To overcome these shortcomings, more and more studies have focused on the use of microwave data (acquired by SAR sensors) to estimate crop BP [21]–[24] or on the use of combined optical and microwave signals [25]–[30]. However, SAR data are not without limitations. They remain complex to interpret since they are sensitive to both soil and vegetation properties (wetness, roughness, phytomass, vegetation structure, etc.).

Regarding the potential use of the main microwave bands (*X*-, *C*-, and *L*-bands), many authors have highlighted the interest

of the *X*- and *L*-bands for the monitoring of wheat [30], [31], corn [27], barley [21], or rice [32]. However, the lack of dense temporal satellite data series acquired at *L*-band and/or their high cost (acquired, for example, by Alos-2, Terrasar-X, Tandem-X, or Cosmoskymed constellation) do not permit their use in fine temporal approaches for crop monitoring. The launch of the European Space Agency's Sentinel satellites from 2015 resolves this limitation in the *C*-band domain. Indeed, they offer an unprecedented opportunity to monitor crops worldwide in both SAR (with Sentinel 1A and 1B) and optical (with Sentinel 2A and 2B) domains at a high temporal frequency and high spatial resolution [33]. Moreover, the multiplicity of Sentinel-1's orbits, which can cover the same field theoretically, offers the opportunity to increase data frequency. In this sense, the feasibility of merging Sentinel-1 data from different orbits deserves to be studied. Regarding optical images, at the field scale, data frequency can also potentially be increased by the combination of different sensors with different features. In particular, Sentinel-2 and Landsat-8 both seem to meet requirements, in terms of spatial resolution, of worldwide field-scale applications.

Nonetheless, most of the few studies that focused on the synergy of optical and SAR data for crop monitoring suffer from the unavailability of a sufficient dense dataset containing concomitant *in situ* and satellite data [27], [34]. Such shortcomings intrinsically weaken the statistical robustness of the relationships established between satellite indicators and *in situ* BP. This is particularly true for rapeseed, for which robust ground measurements are scarce, especially in Europe. However, rapeseed is one of the most important seasonal crops cultivated in the world for oil, proteins, and biofuel production. In 2018, rapeseed was the seventh world crop in terms of cultivated area with almost 37.6 million hectares for a total production of 75 million tons (FAO statistics for 2018).

In this context, the objectives of this study consist in: 1) analyzing the temporal signatures of SAR data from Sentinel-1 and optical data from Sentinel-2 and Landsat-8 throughout the rapeseed crop cycle; 2) analyzing the effect of multiorbit acquisitions on SAR data and multisensor acquisitions on optical data for rapeseed fields; and 3) evaluating the potential of both multiorbital SAR data from Sentinel-1 and multisensor optical data from both Sentinel-2 and Landsat-8 to empirically derive rapeseed BP, i.e., DM, FM, height, and PWC. This article is structured as follows. Section II introduces the material and methods used, including weather data and ground measurements of rapeseed BP in Sections II-A and II-B, respectively, satellites data in Section II-C, and the methodology employed to derive BP from remote sensing indicators (RSI) and evaluate the predictive power of each RSI in Section II-D. Section III is dedicated to the presentation of results. First, the temporal signatures of optical and SAR RSI are analyzed regarding the temporal evolutions of measured BP all along the rapeseed phenological cycle in Section III-A. Second, the feasibility of a fusion of Sentinel-1 data from different orbits is scrutinized through an analysis of angular effects on backscatter coefficients in Section III-B1. In parallel, the sensitivity of optical data to the sensor (Sentinel-2 or Landsat-8) is analyzed in Section III-B2. Finally, relationships between RSI and rapeseed BP are studied and the predictive power of each RSI is analyzed in Section III-C. Results are discussed in Section IV according to the effect of multiorbit and multisensor acquisitions on SAR and optical data, respectively, the impact of fields sampling on empirical relationships, the order of the empirical polynomials functions, and the impact of radiometric correction in SAR processing. Finally, conclusions and perspectives of this work are given in Section V.

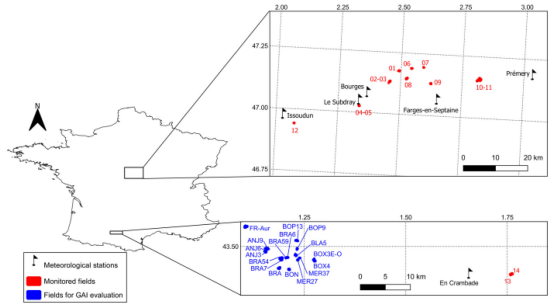

Fig. 1. Map of monitored rapeseed fields (red dots) and those used for GAI measurements (blue dots). Meteorological stations are represented by black flags.

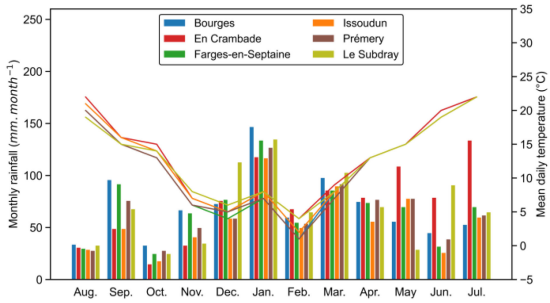

Fig. 2. Ombrothermic diagram of the six meteorological stations for the 2017–2018 agricultural season of rapeseed. Mean daily temperature and monthly rainfall are represented by lines and vertical colored bars, respectively (according to weather station).

II. Material and Methods

A. Description of the Study Sites and Meteorological Conditions

Monitored rapeseed fields used in this study are located in two study sites, specialized in annual grain crops, in southwestern and central France with contrasted pedoclimatic conditions (see Fig. 1). We used meteorological data (i.e., rainfall, temperature, and global radiation) from Météo-France (Issoudun, Le Subdray, Bourges, Farges-en-Septaine, and Prémery stations) and Arvalis Institut du végétal (En Crambade station). These data have been daily acquired by six meteorological stations situated less than 19 km far from the monitored rapeseed fields (see Table I and Fig. 1). Fig. 2 provides an ombrothermic diagram for these six meteorological stations for the entire agricultural season of rapeseed (i.e., from August 2017 to July 2018). Compared to other stations, the southern-most station, i.e., En Crambade, is characterized by milder temperatures, a drier 2017 autumn and a strongly rainier end of the season from May to July 2018. Prémery and Farges-en-Septaine are the coldest stations,

TABLE I
IDENTIFIER, SOWING, AND HARVEST DATES OF MONITORED RAPESEED FIELDS

Field identifier	Sowing date	Harvest date	Nearest meteorological station	Distance from meteorological station (km)	Number of sampling dates	Mean slope (°)
01	2017/08/16	2018/07/03	Bourges	15.57	13	1.9
02	2017/08/22	2018/07/08	Bourges	9.24	13	1.1
03	2017/08/22	2018/07/08	Bourges	9.24	13	1.1
04	No data	No data	Le Subdray	0.71	11	0.4
05	No data	No data	Le Subdray	0.56	11	0.4
06	2017/08/20	2018/06/29	Farges-en-Septaine	17.30	12	1.7
07	2017/08/23	2018/07/18	Farges-en-Septaine	18.57	12	1.6
08	2017/08/16	2018/06/28	Farges-en-Septaine	14.28	12	1.2
09	2017/08/16	2018/07/06	Farges-en-Septaine	9.05	12	1.6
10	2017/08/17	2018/06/29	Prémery	16.29	12	0.6
11	2017/08/19	2018/07/02	Prémery	16.38	12	0.9
12	2017/08/29	2018/07/07	Issoudun	4.15	12	0.7
13	2017/08/27	2018/06/28	En Crambade	8.39	9	2.4
14	2017/08/27	2018/06/28	En Crambade	8.83	9	2.2

For each field, the distance from the nearest meteorological station, the number of ground measurements, and the mean slope are mentioned.

especially during winter. Bourges and Farges-en-Septaine show a rainier autumn. Le Subdray shows significantly higher rainfalls in December and June and winter temperatures comparable to En Crambade. Issoudun has an intermediary behavior.

B. Ground Measurements

In the framework of the R&D project named Colza digital, an intensive field campaign was carried out to collect ground data over 14 fields of winter varieties of rapeseed (*Brassica napus* L.) during the 2017–2018 growing season (see Fig. 1 and Table I).

For each field, *in situ* measurements of crop height, aboveground DM, aboveground FM, and PWC were regularly carried out (20 days timestep on average) from sowing to harvest. For each ground measurement date, three samples of rapeseed plants were collected on a 1 m^2 elementary sampling unit (ESU). All ESUs were located inside a 20 by 30 m^2 area, the center of which was located on average 60 m far from the edge of the field. Aboveground FM was obtained by directly weighing plants on the field. Aboveground DM was obtained after drying plants in an oven (80 °C for 36 h). PWC was obtained from DM and FM. For each BP, the final value is given by averaging measurements performed on the three samples. Phenological stages according to the BBCH scale [35] have also been recorded (see Appendix A). All ground measurements, including BBCH stages, have later been linearly interpolated at a daily time step. Sowing dates vary from August 16 to August 29, 2017, whereas harvest dates vary from June 28 to July 18, 2018 (see Table I).

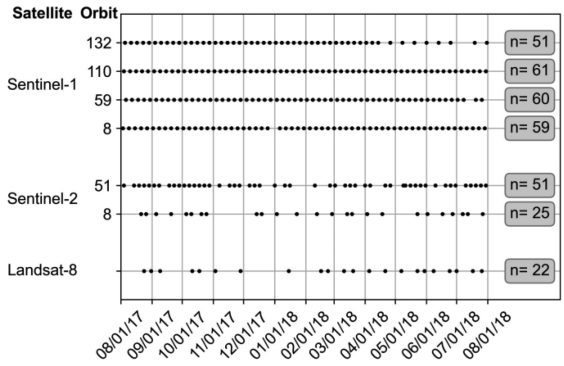

Fig. 3. Chronogram of satellite acquisitions performed in the optical (Sentinel-2, Landsat-8) and microwave (Sentinel-1) domains during the rapeseed crop cycle, according to orbit number: 8, 59, 110, and 132 for Sentinel-1, and 51 and 8 for Sentinel-2 acquisitions. *n* is the number of respective acquisitions.

TABLE II
MAIN FEATURES OF SENTINEL-1 A OR B IMAGES USED IN THIS STUDY

Frequency	5.405 GHz (C-band)
Mode	Interferometric Wide Swath
Product type	Ground Range Detected
Ground range resolution	5 m
Azimuth resolution	20 m
Temporal resolution	12 days
Orbits	Ascending (59, 132) & Descending (8, 110)
Polarization	Dual (VV & VH)
Swath	250 km
Incidence angle	30,3 - 43,5°

In addition to the 14 monitored fields, 18 other independent winter rapeseed fields have been used to evaluate the GAI derived from Sentinel-2 and Landsat-8 images (see blue fields in Fig. 1) and sensor effect on optical data. GAI measurements were carried out on one ESU of 30 by 30 m^2 for each field using the SunScan Canopy Analysis System (Delta-T Devices, Ltd., U.K.) for the FR-Aur field and from hemispherical photography acquired according to the protocol described in [36] and treated with the CAN-EYE software [37] for the other fields (see Appendix B for more details on the features of these fields).

C. Satellite Acquisitions

Fig. 3 shows a chronogram of satellite acquisitions performed in both optical (Sentinel-2, Landsat-8) and microwave (Sentinel-1) domains during the 2017–2018 rapeseed crop season.

1) SAR Data: The backscatter coefficients at *C*-band (5.405 GHz) were provided by the SAR sensor onboard the Sentinel-1 satellite (see Table II). They were derived from the interferometric wide (IW) mode and ground range detected (GRD) processing from four different orbits (i.e., 132, 110, 59, and 8; Fig. 3). Mean incidence angles at field scale are $\theta_{132} = 43.5°$, $\theta_{110} = 38.3°$, $\theta_{59} = 36.6°$, and $\theta_8 = 30.3°$ for the four orbits allowing a repetitiveness of 2.6 days on average for all combined orbits (231 images). Backscatters coefficients for the four orbits and the two polarizations (VH and VV) were extracted for each field (noted $\sigma^0{}_{\mathrm{VH}}$ and $\sigma^0{}_{\mathrm{VV}}$ in the following) from preprocessed GRD data using the Google Earth Engine (GEE) website [38]. The GEE preprocessing includes the following steps: orbit file application, GRD border noise removal, thermal noise removal, radiometric

TABLE III
MAIN FEATURES OF OPTICAL IMAGES USED IN THIS STUDY

Sensors	Sentinel-2	Landsat-8
Bands	B1 (443 nm) B2 (452 - 512 nm), B3(636 - 673 nm), B4 (636 - 673 nm), B5 (851 - 879 nm), B6 (1566 - 1651 nm), B7 (2107 - 2294 nm), B8 (842 nm), B8a (865 nm) B9 (940 nm), B10 (1375), B11 (1610 nm), B12 (2190 nm)	B1 (435 - 451 nm), B2 (452 - 512 nm), B3(636 - 673 nm), B4 (636 - 673 nm), B5 (851 - 879 nm), B6 (1566 - 1651 nm), B7 (2107 - 2294 nm), B9 (1363 - 1384 nm)
Product type	Level-1C Top-Of-Atmosphere reflectance	Level-1 Top-Of-Atmosphere reflectance
Spatial resolution	10 m (B2, B3, B8), 20 m (B5, B6, B7, B8a, B11, B12), 60 m (B1, B9, B10)	30 m
Temporal resolution	5 days	16 days
Orbits	51 & 8	-
Swath	290 km	185 km

calibration (sigma naught), range Doppler terrain correction, and resampling at 10 m spacing. Two indexes were derived from $\sigma^0{}_{\mathrm{VH}}$ and $\sigma^0{}_{\mathrm{VV}}$: the co-cross-polarization ratio ($\sigma^0{}_{\mathrm{VH\text{-}VV}}$) and the radar vegetation index (RVI). Originally introduced in [39], RVI is generally calculated using quadpolarized SAR data. Since Sentinel-1 only provides VH and VV polarizations, RVI was computed according to [40], who adapted the concept of RVI for dual-polarization Sentinel-1 data as follows:

$$\mathrm{RVI} = \frac{4\sigma^0_{\mathrm{VH}}}{\sigma^0_{\mathrm{VV}} + \sigma^0_{\mathrm{VH}}} \tag{1}$$

where $\sigma^0{}_{\mathrm{VH}}$ and $\sigma^0{}_{\mathrm{VV}}$ are the backscatter coefficients in VH and VV polarization, respectively. They are expressed in $\mathrm{m}^2{\cdot}\mathrm{m}^{-2}$, and RVI has no unit.

2) Optical Data: NDVI, fCover, and GAI were calculated from both ESA Sentinel-2 level-1C and USGS Landsat-8 level-1 products (see Table III). fCover and GAI were obtained by inverting the PROSAIL canopy reflectance model [41] with the Overland processor developed by Airbus DS GEO (https://www.intelligence-airbusds.com/verde-processing/). The overland processing principle is based on the coupling of the combined PROSPECT leaf optical properties model [42] and SAIL canopy bidirectional reflectance model [43], [44] with the LOWTRAN 7 atmospheric model [45] completed with an ad-hoc cloud model. Overland uses top of atmosphere radiances as inputs to perform inversion of the above described coupled model through minimization techniques. Thanks to its built-in atmospheric model, overland performs autonomous atmospheric corrections of reflectance as well as automatic masking of thin clouds and dark shadows. The overland processor also includes a coregistration algorithm to deal with differences in native resolutions and geometric performances of Sentinel-2 and Landsat-8. A detailed description of the overland algorithms can be found in [46]. Only fCover, NDVI, and GAI estimations derived from images with more than 80% of cloud-free pixels over considered rapeseed fields were conserved. fCover, NDVI, and GAI were finally derived from 76 Sentinel-2 images and 22 Landsat-8 images for the 14 monitored rapeseed fields throughout the entire rapeseed growth cycle (see Fig. 3). Field-scale fCover, NDVI, and GAI were obtained using the mean value of pixels included in the field.

D. Methodology

First, the temporal signatures of SAR and optical signals were analyzed in light of the temporal evolution of *in situ* BP (see Section III-A). In this study, four orbits from Sentinel-1 have been simultaneously exploited to increase SAR data acquisitions for each studied rapeseed field. Acquisitions from different orbits necessarily induce different angular configurations, which can affect backscatter coefficients values. Consequently, orbital effects on SAR data have been scrutinized (see Section III-B1). Optical data have also been acquired from two different sensors, i.e., Sentinel-2 and Landsat-8, whose impact on the accuracy of GAI estimates was assessed (see Section III-B2).

We then analyzed and evaluated the relationship between both SAR and optical RSI, respectively derived from Sentinel-1 and Sentinel-2 and Landsat-8, and the ground measurements of DM, FM, height, and PWC acquired on the 14 monitored rapeseed fields during the entire 2017–2018 crop cycle (see Section III-C). In the first step regarding SAR RSI aside, evaluation was performed for the complete SAR dataset (see Section III-C1). In the second step, for a fair statistical comparison between optical and SAR RSI, this evaluation was performed for concurrent acquisitions of optical and SAR data (see Section III-C2). We also scrutinized the effect of phenological stages on the suitability of empirical relationships by analyzing the distribution of residuals (i.e., differences between measured and estimated BP) of the best RSI-based relationship by BBCH main stages (see Section III-D).

1) Definition of RSI: Four SAR RSI, i.e., $\sigma^0{}_{\mathrm{VH}}$, $\sigma^0{}_{\mathrm{VV}}$, $\sigma^0{}_{\mathrm{VH\text{-}VV}}$, and RVI, and three optical RSI, i.e., NDVI, fCover, and GAI, have been considered. As an alternative to raw RSI, we proposed new indicators (noted η_{RSI}) based on the cumulative sum of each RSI, and already successfully applied to the estimation of wheat parameters [47]

$$\eta_{\mathrm{RSI}}(d_i) = \sum_{0}^{n} |\mathrm{RSI}(d_i)| \ (d_i - d_{i-1}) \tag{2}$$

where RSI (d_i) is the value of the given RSI at day d_i, n is the total number of remote sensing acquisitions, and ($d_i - d_{i-1}$) is the number of days between day d_i and the previous acquisition date d_{i-1}. This term allows taking into account the differences of acquisition frequency between monitored fields for both SAR (mainly due to orbits configurations) and optical (mainly due to cloud cover conditions) images. For all RSI, a common starting date d_0 is set for all fields for which η_{RSI} is initialized to 0. In this study, d_0 was set to August 4, 2017 for both SAR and optical data, matching the dates of the first presowing available Sentinel-1 image and/or the first presowing available Sentinel-2 or Landsat-8 image. A complete list of RSI analyzed in this article is given in Table IV.

2) Analysis of Orbital Effects on SAR Data: To consider the feasibility of the fusion of Sentinel-1 data from different orbits, we scrutinized angular effects on backscattering coefficients. To

TABLE IV
RSI USED IN THIS STUDY

RSI	Domain	Unit
NDVI	Optical	-
fCover	Optical	%
GAI	Optical	$m^2.m^{-2}$
η_{NDVI}	Optical	days
η_{fCover}	Optical	%.days
η_{GAI}	Optical	$m^2.m^{-2}$.days
σ^0_{VH}	SAR	dB
σ^0_{VV}	SAR	dB
σ^0_{VH-VV}	SAR	dB
RVI	SAR	-
$\eta_{\sigma VH}$	SAR	dB.days
$\eta_{\sigma VV}$	SAR	dB.days
$\eta_{\sigma VH-VV}$	SAR	dB.days
η_{RVI}	SAR	days

do so, we analyzed the temporal evolution of the Γ variable (in $dB \cdot {}^{\circ -1}$) defined as follows:

$$\Gamma = \frac{\Delta\sigma^0}{\Delta\theta} \tag{3}$$

where $\Delta\sigma^0$ (dB) and $\Delta\theta$ (°) are the differences between either σ^0_{VH}, σ^0_{VV} or $\sigma^0_{VH\text{-}VV}$ and the incidence angles from two successive acquisitions in different orbits. Considering the sensitivity of SAR data to soil moisture, in this analysis, we also computed cumulated rainfall values from the nearest meteorological station between two consecutive acquisitions. In this way, we investigated if the difference between σ^0 values can rather be explained by a rainfall event than by a difference in incidence angle.

3) Evaluation of Optical GAI and Analysis of Sensors Effects on Optical Data: To explore the effect of sensors on optical data, two kinds of analysis have been carried out. In the first one, the accuracy of GAI estimations derived from Sentinel-2 and Landsat-8 has been assessed by comparing them with *in situ* measurements acquired on the 18 fields with available ground GAI (see blue fields in Fig. 1). For this comparison, the results were analyzed according to the sensor and according to the time difference between ground measurements and acquisition dates of satellite images.

In a second analysis, GAI, fCover, and NDVI derived from Sentinel-2 and Landsat-8 have been compared with each other for all monitored fields (i.e., blue and red fields in Fig. 1) by considering a maximal difference of one day between acquisition dates of Sentinel-2 and Landsat-8 images.

4) From Satellite to Crop Parameters: Linear (4) and second-order polynomial (5) regressions were established between either SAR or optical indicators and measured BP

$$P = a\mathrm{RSI} + b \tag{4}$$

$$\mathrm{BP} = a\mathrm{RSI}^2 + b\mathrm{RSI} + c \tag{5}$$

where BP is a rapeseed biophysical parameter (DM, FM, PWC, height), RSI is a remote sensing indicator from either SAR or optical domain, and *a, b, c* are the parameters of the regression. Performance of each relationship was evaluated using the coefficient of determination (R^2), root-mean-square error (RMSE), and relative root-mean-square error ($RMSE_r$).

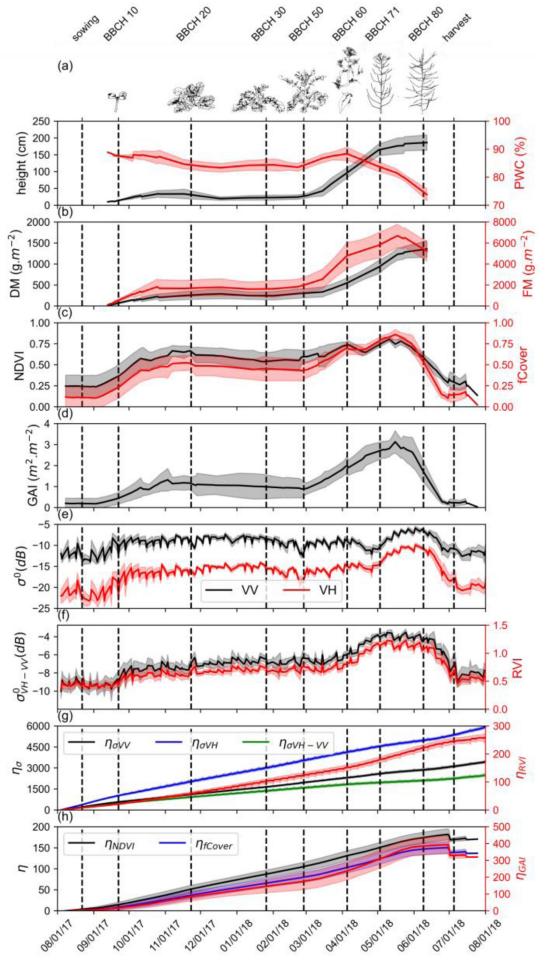

Fig. 4. Temporal evolution of *in situ* (a) height and PWC, (b) DM and FM, (c) optical NDVI and fCover, (d) GAI, (e) SAR backscattering coefficients, and (f) backscattering coefficients ratio and RVI, (g) as well as η_{RVI} and η_σ for VH and VV polarization and VH-VV ratio and (h) η_{NDVI}, η_{fCover}, and η_{GAI}. Lines and shadow areas represent the mean and standard deviation of the considered variable, respectively. The mean of *in situ* observed dates of the main rapeseed phenological stages is given by vertical dashed lines with corresponding stages name and plant illustrations at the top of the panel (a).

III. RESULTS

A. SAR and Optical Temporal Signatures

Fig. 4 shows the temporal evolution of fCover, NDVI [see Fig. 4(c)], GAI [see Fig. 4(d)], σ^0_{VH}, σ^0_{VV} [see Fig. 4(e)], $\sigma^0_{VH\text{-}VV}$ and RVI [see Fig. 4(f)], $\eta_{\sigma VH}$, $\eta_{\sigma VV}$, $\eta_{\sigma VH\text{-}VV}$, η_{RVI} [see Fig. 4(g)], η_{fCover}, η_{NDVI}, η_{GAI} [see Fig. 4(h)], as well as *in situ* measurements of height and PWC [see Fig. 4(a)], DM and FM [see Fig. 4(b)] as the mean and standard deviation of all studied fields. In this figure, for display reasons, ground measurements, optical and radar indicators have been linearly interpolated beforehand at a daily timescale.

1) Optical Signatures: NDVI and fCover showed similar behavior, both rapidly increasing from cotyledon emergence (BBCH 09) to the development of first leaves (BBCH ~13). This increase was steeper than the one showed by *in situ* height, DM, and FM. On the contrary, PWC showed a slight decrease from sowing to the first leaves development. Similar to all,

BP, NDVI, and fCover then stagnated until the end of stem elongation (BBCH 39). However, measured height showed a particular behavior with a winter decrease during the beginning of December where interfield variability is high before decreasing until BBCH 50. Such a winter decrease was clearly attenuated for DM and FM that rather exhibited stagnation. Both NDVI and fCover later increased from BBCH 50 to reach a peak during siliques development (around BBCH 73). This peak was reached earlier than the peak of measured FM. NDVI and fCover finally rapidly decreased until harvests such as *in situ* FM and PWC, whereas height and DM stagnated. Note that during early April, when rapeseed is flowering, NDVI showed a slight decrease, whereas fCover stagnated. Note also that NDVI showed a higher saturation effect than fCover during nongrowing periods (before sowing and after harvest), during which vegetation cover was particularly sparse, even absent.

GAI showed a similar time curve but with higher intra-annual variability. More precisely, the increase during the leaves development (BBCH 10 to 29) was smoother, whereas the increase from inflorescence emergence (BBCH 50) to fruit development (BBCH $\sim$ 73) and the decrease during fruit maturation were steeper. During the peak phase, interfield variability was higher for GAI (coefficient of variation CV $=$ 17.1%) than for NDVI (CV $=$ 6.6%) and fCover (CV $=$ 7.1%). Regarding optical η_{RSI}, they all showed a quasi-linear increase with a slightly higher slope from sowing to the first leaves development and from stem elongation to fruits development, corresponding to an increase in NDVI, fCover, and GAI values.

2) SAR Signatures: Regarding SAR indicators, $\sigma^0{}_{\mathrm{VH}}$ and $\sigma^0{}_{\mathrm{VV}}$ were particularly noisy (CV $=$ 9.0 and 13.7%, respectively) during the beginning of the agricultural season when vegetation cover was less developed. This is probably due to their sensibility to soil moisture and surface roughness at this stage. The use of $\sigma^0{}_{\mathrm{VH\text{-}VV}}$ allowed reducing this noise (CV $=$ 5.9%). $\sigma^0{}_{\mathrm{VH\text{-}VV}}$ and RVI showed very similar behavior. Similar to optical RSI, $\sigma^0{}_{\mathrm{VH}}$, $\sigma^0{}_{\mathrm{VV}}$, $\sigma^0{}_{\mathrm{VH\text{-}VV}}$, and RVI started from low values (around $-$ 22 dB, $-$ 12 dB, $-$ 10 dB, and 0.36, respectively) and increased during the development of the first leaves and rapidly reached a quasi-plateau until the inflorescence emergence. Note that the increase for $\sigma^0{}_{\mathrm{VH\text{-}VV}}$ and RVI was smoother than for $\sigma^0{}_{\mathrm{VH}}$, $\sigma^0{}_{\mathrm{VV}}$. Then, both $\sigma^0{}_{\mathrm{VH\text{-}VV}}$ and RVI increased and reached a new plateau around $-$ 4 dB (respectively 1.2) during fruits development before rapidly decreased during fruits maturation following the desiccation of rapeseed organs, as illustrated by the PWC decrease. Standard deviation increases during this decline due to the variability in the harvest dates. Unlike $\sigma^0{}_{\mathrm{VH\text{-}VV}}$ and RVI, $\sigma^0{}_{\mathrm{VH}}$ and $\sigma^0{}_{\mathrm{VV}}$ showed a slight decrease during flowering. Note also that the decrease during fruits maturation is stronger for $\sigma^0{}_{\mathrm{VH}}$ than for $\sigma^0{}_{\mathrm{VV}}$. Interfields variability was globally smaller for SAR RSI (CV of 8.7% on average) than for optical RSI (CV of 24.1% on average).

Similar to optical η_{RSI}, SAR η_{RSI} showed a quasi-linear increase with a slightly higher slope from sowing to the first leaves development, corresponding to an increase in backscatter coefficients values, and a slightly lower slope (respectively higher) from BBCH 80 to harvest for η_σ (respectively η_{RVI}), corresponding to a decrease in backscatter coefficients values.

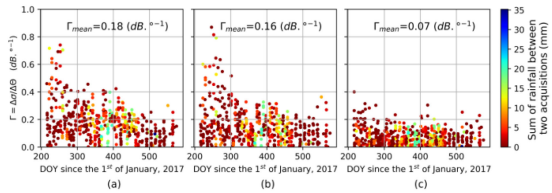

Fig. 5. Temporal evolution of Γ for (a) $\sigma^0{}_{\mathrm{VV}}$, (b) $\sigma^0{}_{\mathrm{VH}}$, and (c) $\sigma^0{}_{\mathrm{VH\text{-}VV}}$. The color of each dot represents the sum of rainfall between two acquisitions in millimeters.

B. Analysis of Orbital and Sensors Effects

1) Feasibility of Sentinel-1 Orbits Fusion: Analysis of Angular Effects on Backscatter Coefficients: Fig. 5 shows the temporal evolution of Γ for all the studied fields for $\sigma^0{}_{\mathrm{VV}}$ [see Fig. 5(a)], $\sigma^0{}_{\mathrm{VH}}$ [see Fig. 5(b)], and $\sigma^0{}_{\mathrm{VH\text{-}VV}}$ [see Fig. 5(c)]. Only data with a difference of acquisition date of one day and a difference of incidence angle superior to 5° have been considered. For the informational purpose, cumulated rainfall between two acquisitions is also given in the color bar. Both $\sigma^0{}_{\mathrm{VV}}$ and $\sigma^0{}_{\mathrm{VH}}$ data showed significant Γ dispersion (standard deviation of 0.13 dB$\cdot^{\circ\text{-}1}$ for both polarization) with values ranging from 0 to 0.74, and 0 to 0.87 dB$\cdot^{\circ\text{-}1}$, respectively, and a mean value superior to 0.15 dB$\cdot^{\circ\text{-}1}$ (0.18 and 0.16 dB$\cdot^{\circ\text{-}1}$, respectively). Particularly high Γ values ($>$0.40 dB$\cdot^{\circ\text{-}1}$) were observed during the first months of the rapeseed crop cycle (from August to November), for which surface heterogeneity was the highest since the soil was not fully covered by the vegetation. For $\sigma^0{}_{\mathrm{VH\text{-}VV}}$, Γ values were less dispersed (standard deviation of 0.06 dB$\cdot^{\circ\text{-}1}$) whatever the considered crop cycle period and mean value was significantly lower (i.e., 0.07 dB$\cdot^{\circ\text{-}1}$). Note that whatever the considered SAR indicator, cumulated rainfall between two acquisitions had not significant impact on Γ values. These results suggest that Sentinel-1 data fusion from multiorbits is practicable for $\sigma^0{}_{\mathrm{VH\text{-}VV}}$, but is subject to higher angular effects for both $\sigma^0{}_{\mathrm{VH}}$ and $\sigma^0{}_{\mathrm{VV}}$, as demonstrated with Radarsat data in [30].

2) Sensitivity of Optical Signal to Sensors: Fig. 6 provides an evaluation of satellite GAI estimates compared to *in situ* measurements for both Landsat-8 [see Fig. 6(a)] and Sentinel-2 [see Fig. 6b)] images. Results are displayed by field (color of points) and according to the number of days between satellites overpasses and ground measurements (size of points) as both acquisitions are not systematically concomitant. Sentinel-2-derived GAI estimates were in good agreement with *in situ* measurements showing R^2 of 0.78 and RMSE of 0.36 m$^2\cdot$m^{-2} with differences between satellite and ground acquisitions varying from 0 to 8 days. Landsat-8 estimates showed lower accuracy with R^2 of 0.78 and RMSE of 0.41 m$^2\cdot$m^{-2}.

For further evaluation of sensor impacts on optical RSI, Fig. 7 provides a comparison between Landsat-8 and Sentinel-2-derived GAI [see Fig. 7(a)], fCover [see Fig. 7(b)], and NDVI [see Fig. 7(c)] with a maximal difference in acquisition date

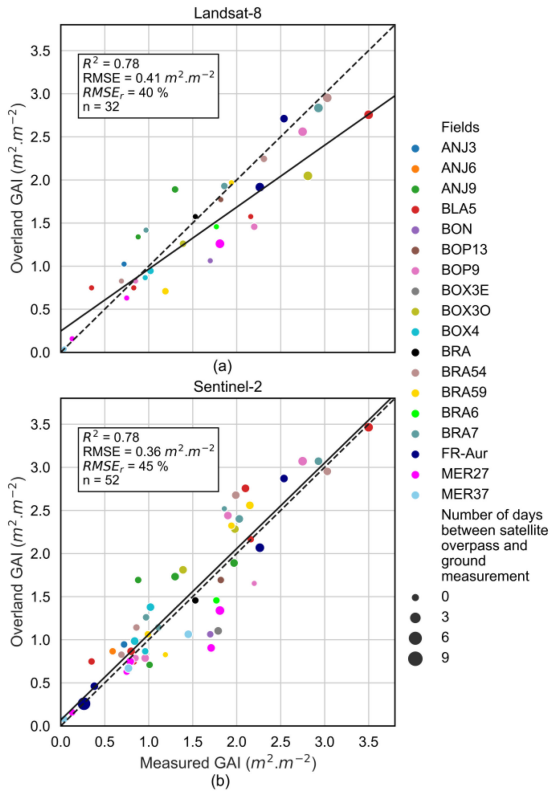

Fig. 6. Comparison between Overland GAI and *in situ* GAI for (a) Landsat-8 and (b) Sentinel-2 images. Dashed line is a 1:1 line and solid line is the linear regression between satellite-derived and measured GAI. The color of points corresponds to the fields' identifiers, whereas their size corresponds to the number of days between satellites overpass and ground measurement. R^2, RMSE, and $RMSE_r$ are given in the top left of each panel.

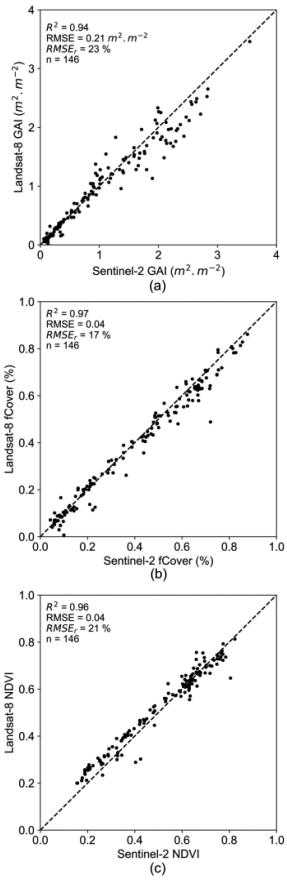

Fig. 7. Comparison between Landsat-8 and Sentinel-2-derived (a) GAI, (b) fCover, and (c) NDVI. Dashed line is a 1:1 line. R^2, RMSE, and $RMSE_r$ are given in the top left of each panel.

of one day. Globally, Landsat-8 and Sentinel-2-derived RSI are in good agreement with R^2 values higher than 0.93 and $RMSE_r$ values below 25%. Landsat-8 estimates showed a slight underestimation for high GAI (>2 $m^2 \cdot m^{-2}$) and fCover (>0.5) values. For NDVI, Landsat-8 showed higher values for low NDVI values (<0.6) and lower values for high NDVI values (>0.6). The combined use of Landsat-8 and Sentinel-2 data allowed an average revisit interval of 12.1 days against 14.2 days for Sentinel-2 acquisitions alone. Moreover, evaluation of Overland GAI from both sensors showed consistent results that permit GAI computation from combined sources.

C. Relationships Between SAR or Optical RSI and Crop BP

1) Comparison Between SAR RSI for Multiorbital Sentinel-1 Acquisitions: Fig. 8 shows the performance of empirical relationships between SAR RSI and rapeseed BP ($n = 1436$). Fig. 9 shows the best relationships obtained between rapeseed BP and SAR RSI. For further information, values of $RMSE_r$ and R^2 for each SAR RSI and each empirical relationship are provided in Appendix C.

Globally, the use of η_{RSI} tended to improve the performance of relationships whatever the RSI considered, except $\sigma^0{}_{VH\text{-}VV}$. Moreover, the second-order polynomial relationship always outperformed simple linear regression. $\sigma^0{}_{VV}$ showed particularly low predictive power whatever the relationship and the BP

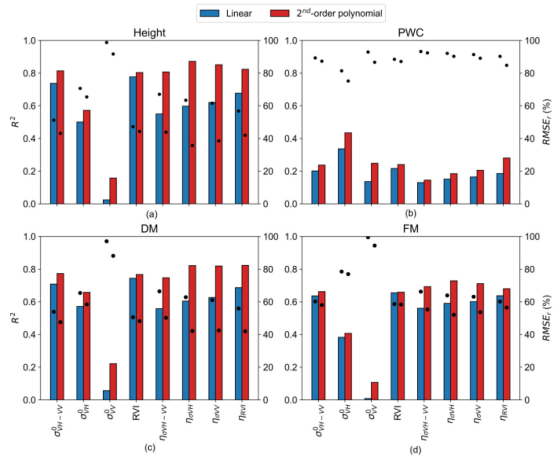

Fig. 8. R^2 (bars) and $RMSE_r$ (dots) of empirical relationships between SAR indicators and *in situ* measured (a) height, (b) PWC, (c) dry mass, and (d) FM.

considered with maximal R^2 values ranging from 0.01 to 0.25 and $RMSE_r$ values ranging from 86.66% to 99.45%.

Regarding height, the best results were obtained with $\eta_{\sigma VH}$ using second-order-polynomial relationship [$R^2 = 0.87$, RMSE = 21.19 cm, and $RMSE_r = 35.73\%$; Figs. 8(a) and 9(a)]. $\eta_{\sigma VV}$ using the second-order polynomial relationship showed

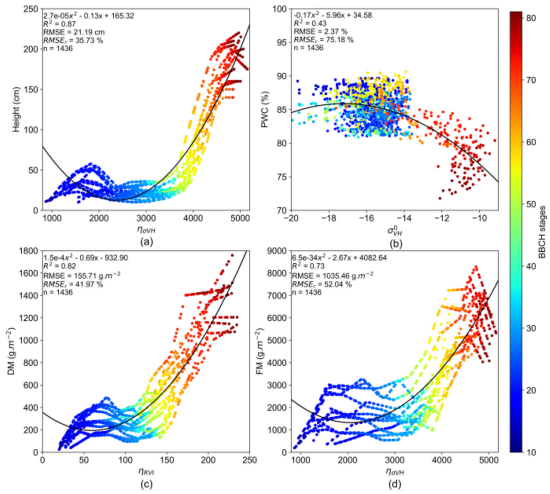

Fig. 9. Best relationships between *in situ* measured (a) height, (b) PWC, (c) DM, and (d) FM and SAR indicators. Equation of the regression as well as values of R^2, RMSE, and $RMSE_r$ and the number of observations (n) are given in the top left corner of each panel.

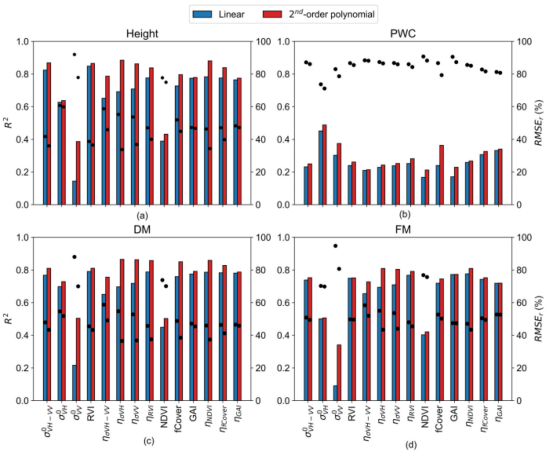

Fig. 10. R^2 (bars) and $RMSE_r$ (dots) of empirical relationships estimated between satellite indicators and *in situ* measured (a) height, (b) PWC, (c) DM, and (d) FM.

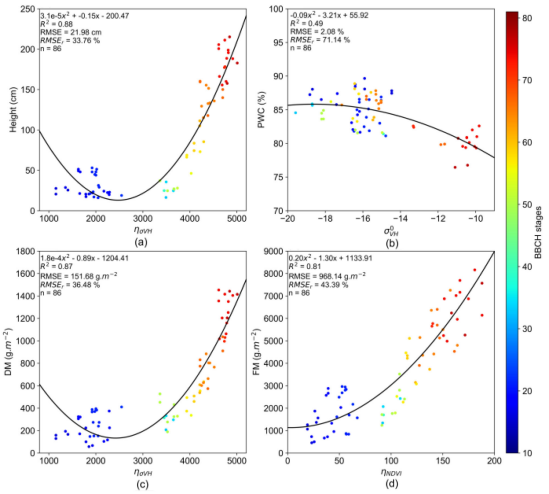

Fig. 11. Best relationships between *in situ* measured (a) height, (b) PWC, (c) DM, and (d) FM and optical RSI. Equation of the regression as well as values of R^2, RMSE, and $RMSE_r$ and the number of observations (n) are given in the top left corner of each panel.

only a slightly lower performance ($R^2 = 0.85$, RMSE = 22.84 cm, and $RMSE_r = 38.51\%$). For PWC, $\sigma^0{}_{VH}$ was the best predictor [$R^2 = 0.60$, RMSE = 2.37%, and $RMSE_r = 63.04\%$ using the second-order polynomial relationship; Figs. 8(b) and 9(b)]. Globally all SAR RSI provided low performance for PWC retrieval.

Regarding DM, η_{RVI} was the best predictor [$R^2 = 0.82$, RMSE = 155.71 g·m^{-2} and $RMSE_r = 41.97\%$ using second-order polynomial relationship; Figs. 8(c) and 9(c)]. Using the second-order polynomial regression, $\eta\sigma_{VH}$ and $\eta\sigma_{VV}$ showed similar performance ($R^2 = 0.82$, RMSE = 156.37 g·m^{-2}, $RMSE_r = 42.15\%$ and $R^2 = 0.82$, RMSE = 157.54 g·m^{-2}, $RMSE_r = 41.97\%$, respectively). Using the second-order polynomial regression, $\eta\sigma_{VH}$ was the best predictor for FM [$R^2 = 0.73$, RMSE = 1035.46 g·m^{-2}, and $RMSE_r = 52.04\%$; Figs. 8(d) and 9(d)] followed by $\eta\sigma_{VV}$ ($R^2 = 0.71$, RMSE = 1068.62 g·m^{-2}, and $RMSE_r = 53.71\%$).

2) Evaluation of SAR and Optical RSI Performances for Concurrent Acquisitions: Fig. 10 shows the overall performance of empirical relationships between RSI and rapeseed BP for SAR and optical concurrent acquisitions ($n = 86$), whereas Fig. 11 focuses on the best relationships. For further information, values of $RMSE_r$ and R^2 for each RSI and each empirical relationship are provided in Appendix D.

Again, the use of η_{RSI} improved the performance of relationships whatever the considered RSI, except $\sigma^0{}_{VH\text{-}VV}$ and GAI. NDVI provided poor results, whatever considered BP. For every BP and every RSI, the second-order polynomial regression outperformed linear regression.

Concerning height, the best results were obtained with $\eta_{\sigma VH}$ using polynomial regression [$R^2 = 0.88$, RMSE = 21.98 cm and $RMSE_r = 33.76\%$; Figs. 10(a) and 11(a)]. η_{NDVI} using the second-order polynomial relationship showed only a slightly lower performance ($R^2 = 0.88$, RMSE = 22.37 cm, and $RMSE_r = 34.35\%$). σ_{VV} and NDVI showed particularly low predictive power whatever the considered relationship with R^2 values below 0.43 and $RMSE_r$ values above 74% (RMSE >48 cm).

For PWC, no RSI provided satisfactory results [$R^2 = 0.17$–0.49 and $RMSE_r = 71.14$–90.71%; Fig. 10(b)] throughout the entire crop cycle. The best performance were obtained with $\sigma^0{}_{VH}$ using the second-order polynomial regression [$R^2 = 0.49$, RMSE = 2.08%, and $RMSE_r = 71.14\%$; Fig. 11(b)]. Regarding DM, $\eta_{\sigma VH}$ was the best predictor using the second-order polynomial regression [$R^2 = 0.87$, RMSE = 151.68 g·m^{-2}, and $RMSE_r = 36.48\%$; Fig. 11(c)]. $\eta_{\sigma VV}$ ($R^2 = 0.86$, RMSE = 153.06 g·m^{-2}, and $RMSE_r = 36.81\%$), η_{RVI} ($R^2 = 0.86$, RMSE = 155.83 g·m^{-2}, and $RMSE_r = 37.48\%$), and η_{NDVI} ($R^2 = 0.86$, RMSE = 155.27 g·m^{-2}, and $RMSE_r = 37.34\%$) showed similar performance [see Fig. 10(c)]. Using the second-order polynomial regression, η_{NDVI} was the best predictor for FM ($R^2 = 0.81$, RMSE = 968.14 g·m^{-2}, and $RMSE_r = 43.39\%$),

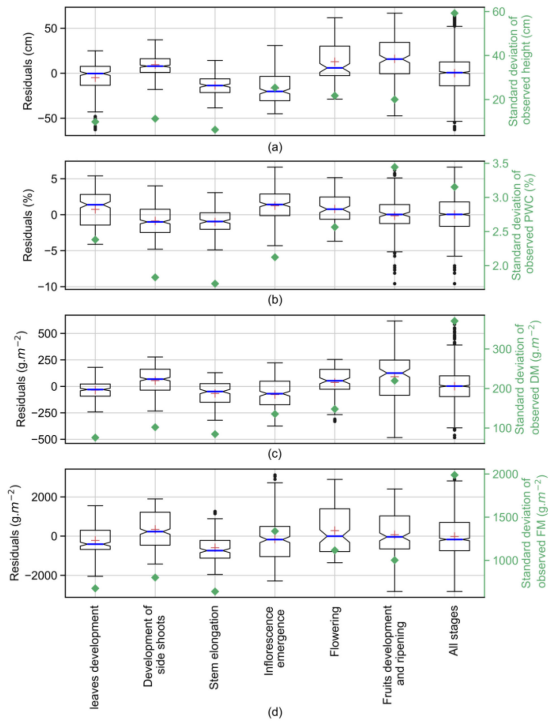

Fig. 12. Boxplots of residuals of the best SAR-based relationship for (a) height, (b) PWC, (c) DM, and (d) FM by main phenological stages. Blue lines and red crosses represent the median and the mean of each distribution, respectively. Green diamonds represent the standard deviation of *in situ* measurements of each BP for the considered main phenological stage.

closely followed by $\eta\sigma_{\mathrm{VH}}$ ($R^2 = 0.81$, RMSE $= 968.23$ g·m^{-2}, and $\mathrm{RMSE_r} = 43.40\%$) [see Figs. 10(d) and 11(d)].

D. Interphenological Stages Variability

Fig. 12 shows the standard deviation in observations (between fields) and boxplots of residuals (i.e., the differences between measured and simulated BP) of the best multiorbit SAR-based relationship for each BP (see Section III-C1). These values are calculated for the main phenological stages and for all stages. Due to the lack of observations for BBCH above 80, fruits development and fruit ripening stages have been clustered.

Regarding height, the interquartile range of residuals was enlarged for inflorescence emergence, flowering and fruits development, and ripening compared to the previous stages [see Fig. 12(a)]. More precisely, residuals were significantly negatively skewed during inflorescence emergence (median of -20.2 and average of -16.7 cm) and positively skewed during flowering (median of 5.9 and average of 12.9 cm) and fruits development and ripening (median of 15.7 and average of 16.0 cm) indicating an overestimation (respectively an underestimation) of rapeseed height. Note that these stages were those associated with the largest standard deviation in observed height.

Regarding PWC, the fruits development and ripening stages showed a particular behavior with a large number of negative outliers resulting in a large overestimation of derived PWC. Note that whatever considered BP, it was the only case for which

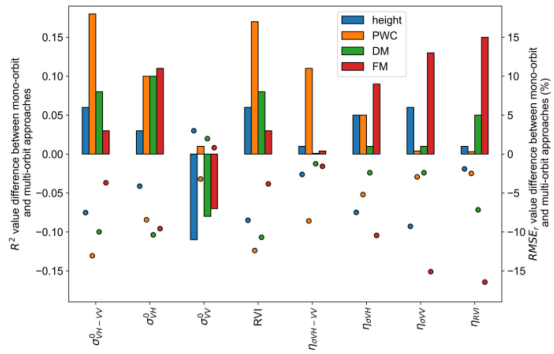

Fig. 13. Differences in R^2 (bars) and $\mathrm{RMSE_r}$ (dots) between mono-orbit and multiorbit SAR-based best relationship for rapeseed BP retrieval.

standard deviation was higher for one phenological stage than for all stages combined. The leaves development stage showed a higher interquartile range and a slightly positively skewed distribution of residuals (median of 1.4 and average of 0.7%).

For DM, interfields variability (i.e., the standard deviation in observations) globally increased with the growth of rapeseed [Fig. 12(c)]. Compared to other stages, residuals distribution was strongly enlarged for fruits development and ripening and showed a negative skewness (median of 125.7 and average of 91.9 g·m^{-2}). Other stages showed a similar interquartile range and a slighter skewness of residuals distribution.

The distribution of residuals for FM was not significantly skewed whatever the considered phenological stage except for stem elongation [see Fig. 12(d)]. A larger distribution was observed for the development of side shoots and inflorescence emergence. The latter was associated with the highest standard deviation in observed FM. The flowering and fruits development and ripening stages also showed a higher interquartile range compared to previous stages.

IV. Discussion

A. Impact of Multiorbit Acquisitions on SAR RSI Predictive Power

Similar to Section III-C1, we performed SAR RSI-based regressions to retrieve rapeseed BP but for mono-orbital (orbit 110) Sentinel-1 acquisitions. We then computed the difference in terms of R^2 and $\mathrm{RMSE_r}$ values between mono-orbit and multiorbit best relationships for each RSI and each BP. Results of this procedure are shown in Fig. 13. Globally, except for $\sigma^0{}_{\mathrm{VV}}$, the mono-orbit approach induced a slight improvement of R^2 and $\mathrm{RMSE_r}$ values. However, differences in performance between mono-orbit and multiorbit approaches remained relatively low. The best improvement was achieved for PWC and FM. Note that for the mono-orbit approach, the best predictors using a second-order polynomial regression are $\eta_{\sigma\mathrm{VH}}$ for height ($R^2 = 0.95$, RMSE $= 21.48$ cm, and $\mathrm{RMSE_r} = 28.25\%$), $\sigma^0{}_{\mathrm{VH}}$ for PWC ($R^2 = 0.53$, RMSE $= 2.39\%$, and $\mathrm{RMSE_r} = 66.74\%$), η_{RVI} for DM ($R^2 = 0.87$, RMSE $= 148.60$ g·m^{-2}, and $\mathrm{RMSE_r} = 34.81\%$) and $\eta_{\sigma\mathrm{VV}}$ for FM ($R^2 = 0.84$, RMSE $= 1107.85$ g·m^{-2}, and $\mathrm{RMSE_r} = 38.60\%$).

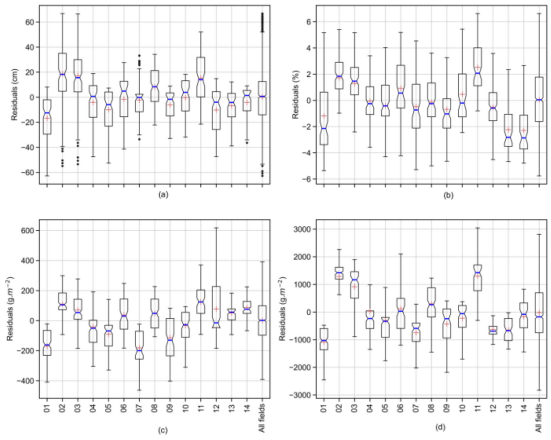

Fig. 14. Boxplots of residuals of the best SAR-based relationship for (a) height (a), (b) PWC, (c) DM, and (d) FM by field. Blue lines and red crosses represent the median and the mean of each distribution, respectively.

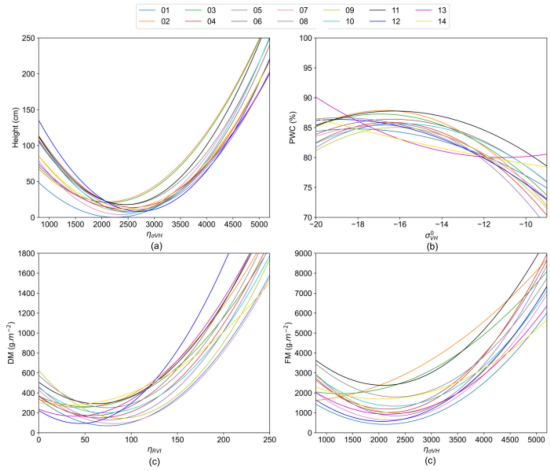

Fig. 15. Best relationships between *in situ* measured (a) height, (PWC) PWC, (c) DM, and (d) FM and SAR indicators for each field taken separately (color code by field identifier).

Furthermore, for three of the biophysical-monitored parameters (i.e., height, PWC, and FM), RSI based on the polarized backscattering coefficients (VV or VH) stood out as being the most efficient, although they showed greater sensitivity to angular effects from orbits fusion than the polarization ratio (see Section III-B1). On the one hand, if the multiorbital approach offered satisfactory results, a slight degradation of statistical performance was observed compared to the mono-orbital approach, whatever BP considered. On the other hand, the multiorbital approach allows to materially increase the number of acquisitions with an average revisit interval of 2.6 days against 6 days for mono-orbital acquisitions (combining Sentinel-1A and B). Hence, the choice between the mono-orbital and multiorbital approach will depend on the objective sought between the statistical accuracy of the empirical relationship and the desired frequency of considered BP estimations.

B. Impact of Fields Sampling on Empirical Relationships

Fig. 14 shows boxplots by fields of residuals of the best multiorbit SAR-based relationship for each BP (see Section III-C1). Important discrepancies could be observed in field-specific residuals distribution. Whatever considered BP, field 01 always showed a negatively skewed distribution of residuals, whereas plots 02, 03, and 11 were associated with a positively skewed distribution. The field showing an average behavior, i.e., the field showing the less skewed distribution and a small interquartile range, varies according to the considered BP. Regarding height, field 07 showed the less skewed distribution of residuals (median of -0.17 cm and mean of -2.22 cm) and the smallest interquartile range. For PWC, field 04 showed the least skewed distribution of residuals (median of $-$ 0.25% and mean of $-$ 0.05%), whereas it was field 10 for DM (median of 31.3 cm and mean of 122.5 g·m^{-2}) and field 06 for FM (median of -27.2 cm and mean of -32.2 g·m^{-2}). Other plots tended to show either positively or negatively skewed distributions of residuals.

These results highlight the importance of the fields sampling strategy adopted to establish relationships between RSI and measured BP. The sample size and variability of *in situ* observations affect the statistical robustness of these relationships. It is, thus, necessary to consider a sufficient range of fields with different situations in terms of climatic conditions and agricultural practices. To illustrate this point, we calculated the best relationship for each field separately, and we showed the variability of obtained relationships in Fig. 15. One can observe that this variability is significant and varies according to the considered BP and phenological stages. In particular, for DM, it increased throughout the rapeseed phenological cycle [see Fig. 15(c)], while it was relatively constant for height and FM [see Fig. 15(a) and (d)] and strongly enlarged for PWC during the beginning and the end of the agricultural season [see Fig. 15(b)].

C. Complementarity and Potential of Combined SAR/Optical-Derived BP for Monitoring and Modeling Fields of Rapeseed

Most of the time, during the core of the rapeseed growth cycle, SAR and optical signals are out of phase (see Section III-B). More precisely, the increase in optical GAI occurred at the beginning of inflorescence emergence (BBCH 50), whereas backscatter coefficients and RVI remained quite stable until BBCH 60 from which volume scattering increases resulting in an increase of $\sigma^0{}_{\text{VH-VV}}$ and RVI. Finally, the GAI peak was raised during the first half of May, whereas backscatter coefficients showed a peak at the end of May around BBCH 80. After flowering, the rapeseed canopy becomes randomly oriented with the fall of leaves and the inset of siliques. Betbeder *et al.* [28] demonstrated that this steep architecture change induces a strong increase in the canopy contribution in volume scattering. This can explain the delayed peak of backscatter coefficients compared to GAI. Indeed, leaves fall induces a decrease of GAI, but the development of fruits, less covering than leaves, contributes to volume scattering. Furthermore, during winter, most of the fields located in Central France showed a slight decrease in GAI (not shown). This decrease is explained by the

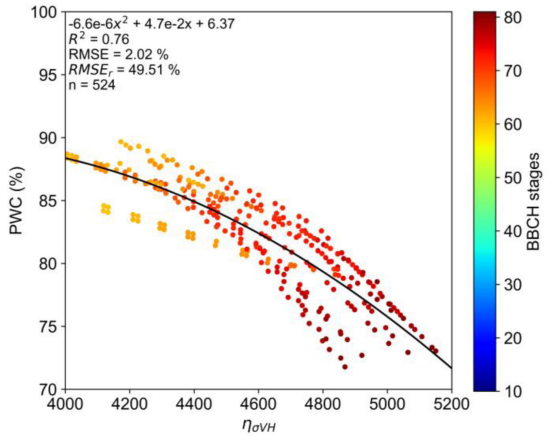

Fig. 16. Best relationship between *in situ* measured PWC and $\eta_{\sigma \mathrm{VH}}$ for BBCH stages beyond 60. Equation of the regression as well as values of R^2, RMSE, and $RMSE_r$ and the number of observations (n) are given in the top left corner of the panel.

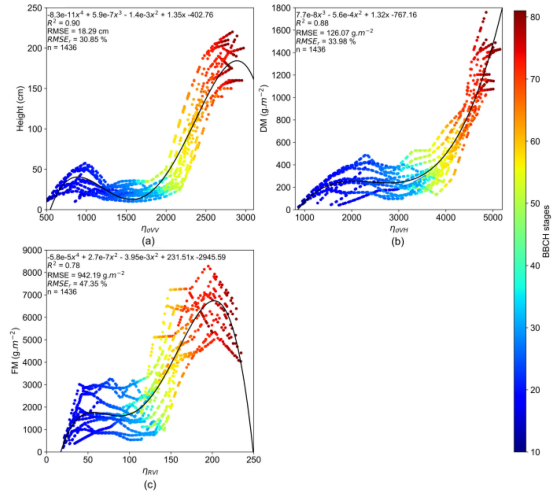

Fig. 17. Best relationships between *in situ* measured (a) height, (b) DM, and (c) FM and SAR indicators for polynomial regression of order 3 or 4. Equation of the regression as well as values of R^2, RMSE, and $RMSE_r$ and the number of observations (n) are given in the top left corner of each panel.

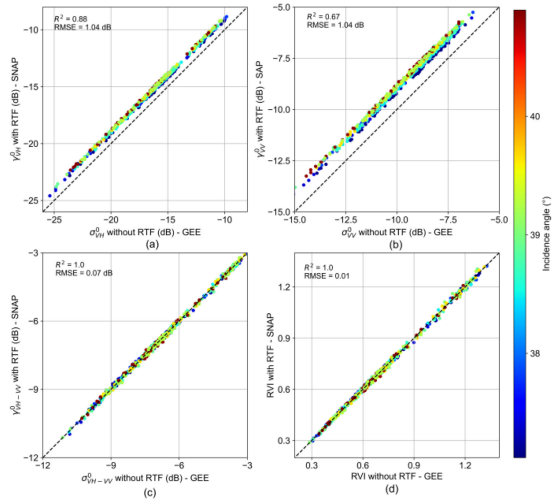

Fig. 18. Comparison between γ^0 with RTF from SNAP and σ^0 without RTF from GEE for (a) VH and (b) VV polarizations, (c) the polarization ratio, and the (d) RVI. The color of points corresponds to the local incidence angle derived from SNAP processing. R^2 and RMSE are given in the top left corner of each panel.

loss of the first well-developed leaves due to winter frosts [48]. Such a phenomenon was not captured in SAR indicators that remained stable during this period.

For the purpose of the assimilation of these remote sensed data in crop models, this complementarity of SAR RSI and optical GAI and the good predictive power of η_{RVI} for DM retrieval are promising. Indeed, in agrometeorological models, GAI and DM are state variables often linked in models formalism (see, e.g., [49]). Consequently, the possibility of driving these two dependent variables by means of independent time series (SAR-derived DM and optically-derived GAI) should provide the right conditions for optimizing rapeseed monitoring and yields modeling. Benefits of combined assimilation of optically-derived GAI and SAR-derived DM in agrometeorological models have been already proved for maize [25], [26], soybean [50], [51], or sunflower [52] but remained to be demonstrated for rapeseed. Besides, the analysis of residuals distribution by phenological stages carried out in Section III-D offered the opportunity to develop an assimilation strategy by periods through a weighing scheme according to the confidence in SAR and/or optical-based relationship for each phenological stage.

D. Performance of RSI-Based Relationship for BP Retrieval in Light of Relevant Previous Studies

Newly introduced SAR η_{RSI} provided very satisfactory results for DM (with η_{RVI}) and height (with $\eta_{\sigma \mathrm{VH}}$) with R^2 above 0.82 and $RMSE_r$ below 42%. For FM, results are more lukewarm with higher interfields variability resulting in higher $RMSE_r$ (52.04%). Globally no clear relationship can be inferred from the comparison of RSI with PWC measurements. However, results for PWC retrieval can be drastically improved ($R^2 = 0.76$, RMSE $= 2.02\%$, and $RMSE_r = 49.51\%$) by using $\eta_{\sigma \mathrm{VH}}$ and considering ground measurements from inflorescence emergence (BBCH 60) only when vegetation starts drying out (see Fig. 16).

The performance of the fitting between SAR RSI and measured BP can also be improved using n-order polynomial regression (third and fourth-order polynomial regressions have been tested; Fig. 17). Table V provides the values of the Akaike Information Criterion (AIC [53]) for each rapeseed BP and each tested regression for the best RSI. Note that the best RSI changed when n-order polynomial regressions are considered. The best improvement is achieved for DM, $\eta_{\sigma \mathrm{VH}}$ being the best RSI [$R^2 = 0.88$, RMSE $= 126.07\ \mathrm{g{\cdot}m^{-2}}$ and $RMSE_r = 33.98$; Fig. 17(b)] using the third-order polynomial regression (a decrease of skill scores is observed for the fourth-order polynomial regression; Table V). For height [$R^2 = 0.90$, RMSE $= 18.29$ cm, and $RMSE_r = 30.85\%$ with $\eta_{\sigma \mathrm{VV}}$; Fig. 17(b)] and FM [$R^2 = 0.78$, RMSE $= 942.19\ \mathrm{g{\cdot}m^{-2}}$ and $RMSE_r = 47.35\%$ with η_{RVI}; Fig. 17(c)], the improvement is lower and required a fourth-order polynomial regression. The use of these n-order relationships reduces the

TABLE V
VALUES OF AIC OF THE RELATIONSHIPS (ORDER 1 TO 4) BETWEEN THE BEST INDICATOR AND EACH RAPESEED BP

	Height	PWC	DM	FM
Linear	13649/RVI	6787/σ^0_{VH}	19112/RVI	24362/RVI
2nd-order polynomial	12851/$\eta_{\sigma VH}$	6561/σ^0_{VH}	18579/η_{RVI}	24020/$\eta_{\sigma VH}$
3rd-order polynomial	12647/$\eta_{\sigma VH}$	6057/η_{RVI}	**17974**/$\eta_{\sigma VH}$	24007/$\eta_{\sigma VH}$
4th-order polynomial	**12433**/$\eta_{\sigma VV}$	**6051**/η_{RVI}	18023/$\eta_{\sigma VH}$	**23753**/η_{RVI}

The best indicator is given after each AIC value and the lower AIC value for each parameter is given in bold.

TABLE VI
VALUES OF RMSE AND R^2 OF THE BEST RELATIONSHIP BETWEEN SAR η_{RSI} DERIVED FROM σ^0 OR γ^0 ACQUIRED IN ORBIT 110 AND RAPESEED BP

	Best relationship with σ^0		Best relationship with γ^0	
	RMSE	R^2	RMSE	R^2
Height (cm)	16.3	0.93	16.3	0.93
PWC (%)	1.7	0.74	1.7	0.74
DM ($g.m^{-2}$)	126.1	0.90	125.7	0.90
FM ($g.m^{-2}$)	951.6	0.79	952.2	0.79

The best skill scores were obtained from fourth-order polynomial regressions using η_{RVI} for height, PWC, and DM and using $\eta\sigma_{VH\text{-}VV}$ ($\eta\gamma_{VH\text{-}VV}$ respectively) for FM.

skill scores difference between mono-orbital and multiorbital approaches (not shown).

Unlike other crops, in particular winter wheat, studies focusing on the potential of SAR and/or optical data to derive BP of rapeseed are scarce, limiting comparison with relevant studies. Direct comparison between studies is particularly tricky due to differences in remote sensed indicators set compared, sensors used, and phenological stages range available from ground measurements.

Using Radarsat-2 quad-polarization data acquired over four rapeseed fields in Southwest France, [30] showed that $\sigma^0_{HV\text{-}HH}$ was the best predictor for crop height using linear regression ($R^2 = 0.76$, $RMSE_r = 43\%$, $n = 36$), notably outperforming σ^0_{VV} ($R^2 = 0.58$, $RMSE_r = 71\%$, $n = 32$) and σ^0_{VH} ($R^2 = 0.44$, $RMSE_r = 80\%$, $n = 40$). However, they obtained better statistical performance with NDVI derived from SPOT-4/5 and Formosat-2 images ($R^2 = 0.82$, $RMSE_r = 25\%$, $n = 26$). For the same fields, Betbeder *et al.* [28] studied the predictive power of polarimetric parameters derived from 14 quad-polarization Radarsat-2 images and NDVI derived from 16 optical images from Formosat-2 and Spot 4/5 sensors. Using an exponential regression, authors obtained the best results with RVI for DM monitoring ($R^2 = 0.8$, $RMSE_r = 7\%$, $n = 9$) and the degree of polarization for height monitoring ($R^2 = 0.67$, $RMSE_r = 15\%$, $n = 40$) both largely outperforming optically-derived NDVI. Using Radarsat-2 quadpolarization wide mode SAR data from eight images acquired over seven rapeseed fields in southern Manitoba (Canada), Wiseman *et al.* [24] obtained the best correlation with entropy using logarithmic regression for DM ($R^2 = 0.65$, $n = 64$). The authors also showed a saturation of the *C*-band signal for dry mass beyond 800 $g{\cdot}m^{-2}$. Using compact polarimetric data from five Radarsat-2 images acquired over 11–14 rapeseed fields (according to the date), Zhang *et al.* [54] showed the potential of Stokes parameters to derive DM ($R^2 = 0.77$) and stem height ($R^2 = 0.92$) using second-order polynomial regressions. Authors showed a nonnegligible improvement of predicted DM ($R^2 = 0.93$, $n = 30$) and height ($R^2 = 0.95$, $n = 22$) using a Random Forest model and 27 compact polarimetric parameters. For the same dataset, and using fully polarimetric data, Yang *et al.* [55] obtained the best results with the ratio between volume scattering and the sum of odd and double-bounce scattering for both DM ($R^2 = 0.85$, $n = 24$) and FM ($R^2 = 0.76$, $n = 36$). Note that these studies concerned summer varieties with low biomass production and a shorter life-cycle without wintering stage compared to our winter rapeseed fields. Such differences jeopardize the direct comparison of the results.

From Sentinel-1 images acquired over three fields in Austria ($n = 25$), Vreugdenhil *et al.* [23] showed that $\sigma^0_{VH\text{-}VV}$ was the best predictor for PWC ($R^2 = 0.34$), FM ($R^2 = 0.34$), and crop height ($R^2 = 0.51$). More recently, using Gaussian processes regression with Sentinel-1 and Sentinel-2 images for a drastically smaller dataset (three rapeseed fields, five dates), Mercier *et al.* [34] demonstrated that $\sigma^0_{VH\text{-}VV}$ was the best SAR indicator to derive DM ($R^2 = 0.80$) and FM ($R^2 = 0.75$), whereas σ^0_{VH} was the best indicator for PWC ($R^2 = 0.60$). However, authors obtained better results using band 11 of Sentinel-2 for DM ($R^2 = 0.85$) and FM ($R^2 = 0.77$).

Globally, the results of this article are in line with these previous studies demonstrating the high potential of *C*-band SAR data for rapeseed BP monitoring, in particular for height and DM. Compared to these studies, we introduced new indicators based on the cumulated sum of backscatter coefficients, polarization ratio, or RVI that proved to significantly improve performances of rapeseed BP retrieval (see Figs. 8 and 10). These indicators allow for the integration of backscattering phenomena over time and are, thus, intrinsically less sensitive to sudden changes (crop architecture, soil moisture due to rainfall or irrigation, dew, etc.) between two acquisitions. Moreover, the present work offered increased robustness of the developed statistical relationship (14 fields, $n = 1436$) and a potential ranking by phenological stages. For instance, we pointed out that the best relationship for DM based on η_{RVI} showed significantly larger residuals distribution for postflowering stages, suggesting that confidence in the developed relationship is impaired for these stages. Such seasonal information should be exploited by providing a dynamic uncertainty or confidence interval of BP estimations according to the considered phenological stage.

E. Impacts of Radiometric Terrain Flattening (RTF) in SAR Data Processing

The backscatters generated by GEE preprocessing are not fully corrected from the terrain deformation as they do not undergo an RTF process. This can introduce bias in radiometric values due to the topographical properties of each field combined with the tilt of the SAR antenna onboard Sentinel-1. The impact of the RTF processing has been evaluated by comparing the sigma backscatters (σ^0) derived from GEE and preprocessed gamma backscatters (γ^0 being the ratio between σ^0 and the cosine of the incidence angle) using the SNAP software (ESA Sentinel Application Platform v8; http://step.esa.int) in VV and VH polarizations as well as for derived polarization ratios and RVI from acquisitions in orbit 110 (see Fig. 18).

Results show that the use of γ^0 with RTF instead of σ^0 without RTF has a significant impact on values derived in VH and VV polarizations ($R^2 = 0.88$ and 0.67, respectively with RMSE $= 1.04$ dB for both polarizations). These differences become negligible for RVI and the polarization ratio ($R^2 = 1$ and RMSE $= 0.01$ and 0.07 dB, respectively). The effect of local incidence angle (derived from the SNAP processing) is more visible for the VV polarization than for the VH polarization (the differences in backscatter values increasing with the local incidence angle). Note that the comparison between γ^0 with and without RTF (all other processing being identical) shows the negligible impact of the RTF processing ($R^2 = 1$, RMSE $= 0.12$ dB for VV and VH polarization, RMSE $= 0.001$ dB for the polarization ratio, and 0.005 for RVI).

The impact of the use of γ^0 with RTF processing rather than σ^0 on the here established relationships between SAR RSI and BP has been assessed. This impact is significant on the relationships based on noncumulated VH and VV backscatters, but slighter for the polarization ratio and RVI (the use of γ^0 inducing a systematic improvement of skill scores; not shown). Finally, when cumulative sums (η_{RSI}) are used, these impacts become totally negligible and the skill scores remain similar whatever the order of the considered polynomial relationship (see Table VI).

V. Conclusion

This article aimed to evaluate the potential of multiorbital SAR and multisensor optical remote sensed data for rapeseed monitoring and the retrieval of its key BP. We introduced new indicators based on the cumulative sum of each RSI (noted η_{RSI}). We showed that the use of η_{RSI} allowed us to significantly improve the predictive power of each indicator, whatever BP considered. The best results were obtained with $\eta_{\sigma\mathrm{VH}}$ for height ($R^2 = 0.87$, RMSE $= 21.19$ cm, $\mathrm{RMSE_r} = 35.73\%$), FM ($R^2 = 0.73$, RMSE $= 1035.46$ g·m^{-2}, $\mathrm{RMSE_r} = 52.04\%$), and PWC ($R^2 = 0.76$, RMSE $= 2.37\%$, $\mathrm{RMSE_r} = 49.51\%$ for postinflorescence emergence stages only) and η_{RVI} for DM ($R^2 = 0.82$, RMSE $= 155.71$ g·m^{-2}, $\mathrm{RMSE_r} = 41.97\%$). We also demonstrated that multiorbital Sentinel-1 SAR data could be used with low impact on the performance of SAR-based relationships allowing to divide by more than two the mean revisit interval. Finally, the asynchronous behaviors of GAI and backscattering coefficients from inflorescence emergence to fruits ripening suggest complementarity between both optical and SAR domains. To further evaluate their robustness, here developed relationships will be tested for other rapeseed fields for which ground datasets have been acquired during the 2018–2019 and 2019–2020 crop seasons in the framework of the Colza Digital project. The use of polarimetric indicators based on fully and compact SAR images should also be investigated on summer rapeseed, as illustrated in [54] and [55]. An assimilation scheme in an agrometeorological model will be later developed for combined SAR and optical remote sensing data-driven rapeseed yields modeling. In a near-real-time simulations perspective, such an approach could be extremely useful to develop insurance products allowing to strengthen financial protection of farmers.

Appendix

Appendix A: BBCH Scale of Main Phenological Stages of Rapeseed

BBCH	Main stages
00	Germination
10	Leaves development
20	Development of side shoots
30	Stem elongation
50	Inflorescence emergence
60	Flowering
70	Fruits development
80	Fruits ripening
90	Senescence

Appendix B: Features of Rapeseed Fields Used for GAI Evaluation

Field identifier	Measurements method	Number of sampling	Sampling dates
FR-Aur	SunScan	5	2018/01/09, 2018/02/27, 2018/03/26, 2018/04/18, 2018/05/09
ANJ9	Hemispherical photography	5	2017/11/29, 2018/03/01, 2018/04/05, 2018/05/02, 2018/05/28
ANJ6	Hemispherical photography	2	2017/11/28, 2018/03/01
ANJ3	Hemispherical photography	1	2017/11/28
BRA54	Hemispherical photography	5	2017/11/28, 2018/03/01, 2018/04/06, 2018/05/04, 2018/05/28
BRA7	Hemispherical photography	5	2017/11/28, 2018/03/01, 2018/04/06, 2018/05/04, 2018/05/28
BRA	Hemispherical photography	1	2017/11/28
BON	Hemispherical photography	1	2017/11/28
MER27	Hemispherical photography	5	2017/11/28, 2018/02/27, 2018/04/05, 2018/05/04, 2018/05/28
MER37	Hemispherical photography	3	2017/11/28, 2018/02/27, 2018/05/28
BOX4	Hemispherical photography	3	2017/11/28, 2018/02/27, 2018/04/04
BOX3E	Hemispherical photography	1	2018/02/27
BOX3O	Hemispherical photography	4	2017/11/28, 2018/04/04, 2018/05/04, 2018/05/28,
BLA5	Hemispherical photography	6	2017/11/28, 2018/02/27, 2018/04/05, 2018/05/28
BOP9	Hemispherical photography	5	2017/11/28, 2018/02/27, 2018/04/06, 2018/05/04, 2018/05/28
BOP13	Hemispherical photography	1	2017/11/28
BRA6	Hemispherical photography	1	2017/11/28
BRA59	Hemispherical photography	5	2017/11/27, 2018/03/01, 2018/04/05, 2018/05/04, 2018/05/28

APPENDIX C:
$RMSE_R$ (%)/R^2 VALUES OF REGRESSIONS BETWEEN RAPESEED BP AND SAR RSI FOR MULTIORBITAL SENTINEL-1 ACQUISITIONS ($N = 1436$)

	σ_{VH-VV}	σ_{VH}	σ_{VV}	RVI	$\eta_{\sigma VH-VV}$	$\eta_{\sigma VH}$	$\eta_{\sigma VV}$	η_{RVI}
				Height (cm)				
Linear	51.22 / 0.74	70.65 / 0.50	98.74 / 0.02	47.20 / 0.78	67.04 / 0.55	63.41 / 0.60	61.56 / 0.62	56.76 / 0.68
2nd-order polynomial	43.11 / 0.81	65.39 / 0.57	91.72 / 0.16	44.30 / 0.80	43.85 / 0.81	35.73 / 0.87	38.51 / 0.85	41.97 / 0.82
				PWC (%)				
Linear	89.32 / 0.20	73.66 / 0.45	92.91 / 0.14	88.48 / 0.22	93.25 / 0.13	92.09 / 0.15	91.37 / 0.16	90.24 / 0.19
2nd-order polynomial	87.29 / 0.24	75.18 / 0.43	86.66 / 0.25	87.12 / 0.24	92.41 / 0.15	90.27 / 0.18	89.11 / 0.21	84.77 / 0.28
				DM ($g.m^{-2}$)				
Linear	53.93 / 0.71	65.41 / 0.57	97.08 / 0.06	50.57 / 0.74	66.44 / 0.56	62.86 / 0.60	61.07 / 0.63	55.92 / 0.69
2nd-order polynomial	47.57 / 0.77	58.43 / 0.66	88.18 / 0.22	48.20 / 0.77	50.24 / 0.75	42.15 / 0.82	42.46 /0.82	41.97 /0.82
				FM ($g.m^{-2}$)				
Linear	60.24 / 0.64	78.52 / 0.38	99.54 / 0.01	58.65 / 0.66	66.26 / 0.56	63.95 / 0.59	63.15 / 0.60	60.20 / 0.64
2nd-order polynomial	58.07 / 0.66	76.98 / 0.41	94.45 / 0.11	58.36 / 0.66	55.35 / 0.69	52.04 / 0.73	53.71 / 0.71	56.50 / 0.68

APPENDIX D:
$RMSE_R$ (%)/R^2 VALUES OF REGRESSIONS BETWEEN RAPESEED BP AND RSI FOR SAR AND OPTICAL CONCURRENT ACQUISITIONS ($N = 86$)

	σ_{VH-VV}	σ_{VH}	σ_{VV}	RVI	$\eta_{\sigma VH-VV}$	$\eta_{\sigma VH}$	$\eta_{\sigma VV}$	η_{RVI}	NDVI	fCover	GAI	η_{NDVI}	η_{fCover}	η_{GAI}
							Height (cm)							
Linear	41.68 / 0.82	60.71 / 0.63	91.98 / 0.14	38.73 / 0.85	58.71 / 0.65	55.20 / 0.69	53.69 / 0.71	47.04 / 0.78	77.69 / 0.39	51.95 / 0.73	47.25 / 0.77	46.32 / 0.78	47.08 / 0.78	48.25 / 0.76
2nd-order polynomial	36.03 / 0.87	59.87 / 0.64	77.86 / 0.39	36.53 / 0.87	45.89 / 0.79	33.76 / 0.88	36.87 / 0.86	40.04 / 0.84	74.96 / 0.43	44.88 / 0.80	46.73 / 0.78	34.35 / 0.88	39.86 / 0.84	47.20 / 0.77
							PWC (%)							
Linear	87.14 / 0.23	73.66 / 0.45	83.02 / 0.30	86.66 / 0.24	88.38 / 0.21	87.32 / 0.23	86.77 / 0.24	85.98 / 0.25	90.71 0.17	86.68 / 0.24	90.53 / 0.17	85.58 / 0.26	82.79 / 0.31	81.27 / 0.33
2nd-order polynomial	86.11 / 0.25	71.14 / 0.49	78.61 / 0.37	85.46 / 0.26	88.14 / 0.21	86.50 / 0.24	85.97 / 0.25	84.28 / 0.28	88.23 / 0.21	79.31 / 0.36	87.29 / 0.23	85.09 / 0.27	81.63 / 0.33	80.76 / 0.34
							DM ($g.m^{-2}$)							
Linear	47.88 / 0.77	54.60 / 0.70	88.01 / 0.22	45.47 / 0.79	58.77 / 0.65	54.73 / 0.70	52.81 / 0.72	45.76 / 0.79	73.80 / 0.45	48.80 / 0.76	47.12 / 0.78	45.94 / 0.79	46.33 / 0.78	46.52 / 0.78
2nd-order polynomial	43.30 / 0.81	51.78 / 0.73	70.00 / 0.50	43.25 / 0.81	49.11 / 0.76	36.48 / 0.87	36.81 / 0.86	37.48 / 0.86	70.11 / 0.50	38.47 / 0.85	45.38 / 0.79	37.34 / 0.86	41.22 / 0.83	45.83 / 0.79
							FM ($g.m^{-2}$)							
Linear	50.85 / 0.74	70.23 / 0.50	94.79 / 0.09	49.74 / 0.75	58.39 / 0.66	55.00 / 0.69	53.61 / 0.71	47.94 / 0.77	76.84 / 0.40	52.70 / 0.72	47.44 / 0.77	47.02 / 0.78	41.22 / 0.83	52.73 / 0.72
2nd-order polynomial	49.43 / 0.75	69.84 / 0.51	80.67 / 0.34	49.57 / 0.75	51.92 / 0.73	43.40 / 0.81	44.00 / 0.80	45.44 / 0.79	75.66 / 0.42	50.15 / 0.75	47.38 / 0.77	43.39 / 0.81	49.45 / 0.75	52.65 / 0.72

ACKNOWLEDGMENT

The authors would like to thank farmers for granting access to their fields. Thanks are also due for B. Garric and D. Poisson from Terres Inovia, H. Gibrin from CESBIO, and P. Corcelles from Axéréal for ground data gathering. These data were acquired as part of a partnership project called "Colza digital" associating Terres Inovia, the Terrena and Axéréal cooperatives, Airbus Defense and Space, the CESBIO, Hiphen, and Wiuz. They would like to thank T. Tallec, F. Granouillac, and H. Gibrin from CESBIO for the acquisition of in situ measurements of GAI. They would also like to thank A. Meillet and F. Hélen from Airbus Defense and Space Geo for their help in Overland data processing and retrieval. Finally, they warmly thank S. Laburthe for proofreading and grammar and language checking of this article. The authors also wish to thank the three anonymous reviewers for their valuable comments. Data acquisitions at the FR-Aur site are mainly funded by the Institut National des Sciences de l'Univers (INSU) through the ICOS ERIC and the OSR SW observatory.

REFERENCES

[1] H. C. J. Godfray *et al.*, "Food security: The challenge of feeding 9 billion people," *Science*, vol. 327, no. 5967, Art. no. 5967, Feb. 2010, doi: 10.1126/science.1185383.

[2] J. Pretty *et al.*, "The top 100 questions of importance to the future of global agriculture," *Int. J. Agric. Sustain.*, vol. 8, no. 4, Nov. 2010, Art. no. 4, doi: 10.3763/ijas.2010.0534.

[3] P. C. Robert, "Precision agriculture: A challenge for crop nutrition management," in *Progress in Plant Nutrition: Plenary Lectures of the XIV International Plant Nutrition Colloquium: Food security and Sustainability of Agro-Ecosystems Through Basic and Applied Research*, W. J. Horst *et al.*, Eds. Dordrecht, The Netherlands: Springer, 2002, pp. 143–149, doi: 10.1007/978-94-017-2789-1_11.

[4] M. Peña-Gallardo *et al.*, "Response of crop yield to different time-scales of drought in the United States: Spatio-temporal patterns and climatic and environmental drivers," *Agric. Forest Meteorol.*, vol. 264, pp. 40–55, Jan. 2019, doi: 10.1016/j.agrformet.2018.09.019.

[5] L. Wang *et al.*, "Growth and yield responses of drip-irrigated cotton to two different methods of simulated hail damages," *Arch. Agron. Soil Sci.*, Aug. 2020, doi: 10.1080/03650340.2020.1789967.

[6] J. Zhang *et al.*, "Monitoring plant diseases and pests through remote sensing technology: A review," *Comput. Electron. Agric.*, vol. 165, Oct. 2019, Art. no. 104943, doi: 10.1016/j.compag.2019.104943.

[7] A. Sharifi, "Using Sentinel-2 data to predict nitrogen uptake in maize crop," *IEEE J. Sel. Topics Appl. Earth Obs. Remote Sens.*, vol. 13, pp. 2656–2662, May 2020, doi: 10.1109/JSTARS.2020.2998638.

[8] M. Battude *et al.*, "Modeling water needs and total irrigation depths of maize crop in the south west of france using high spatial and temporal resolution satellite imagery," *Agric. Water Manage.*, vol. 189, pp. 123–136, Jul. 2017, doi: 10.1016/j.agwat.2017.04.018.

[9] J. Huang *et al.*, "Assimilation of remote sensing into crop growth models: Current status and perspectives," *Agric. Forest Meteorol.*, vol. 276/277, Oct. 2019, Art. no. 107609, doi: 10.1016/j.agrformet.2019.06.008.

[10] X. Jin *et al.*, "A review of data assimilation of remote sensing and crop models," *Eur. J. Agron.*, vol. 92, pp. 141–152, Jan. 2018, doi: 10.1016/j.eja.2017.11.002.

[11] C. Atzberger, "Advances in remote sensing of agriculture: Context description, existing operational monitoring systems and major information needs," *Remote Sens.,* vol. 5, no. 2, Feb. 2013, Art. no. 2, doi: 10.3390/rs5020949.

[12] A. Bégué *et al.*, "Remote sensing and cropping practices: A review," *Remote Sens.,* vol. 10, no. 1, Jan. 2018, Art. no. 99, doi: 10.3390/rs10010099.

[13] H. McNairn and J. Shang, "A review of multitemporal synthetic aperture radar (SAR) for crop monitoring," in *Multitemporal Remote Sensing: Methods and Applications*, Y. Ban, Ed. Cham, Switzerland: Springer, 2016, pp. 317–340, doi: 10.1007/978-3-319-47037-5_15.

[14] D. J. Mulla, "Twenty five years of remote sensing in precision agriculture: Key advances and remaining knowledge gaps," *Biosyst. Eng.*, vol. 114, no. 4, pp. 358–371, Apr. 2013, 10.1016/j.biosystemseng.2012.08.009.

[15] S. C. Steele-Dunne, H. McNairn, A. Monsivais-Huertero, J. Judge, P.-W. Liu, and K. Papathanassiou, "Radar remote sensing of agricultural canopies: A review," *IEEE J. Sel. Topics Appl. Earth Obs. Remote Sens.*, vol. 10, no. 5, pp. 2249–2273, May 2017.

[16] J. Liu, E. Pattey, and G. Jégo, "Assessment of vegetation indices for regional crop green LAI estimation from landsat images over multiple growing seasons," *Remote Sens. Environ.*, vol. 123, pp. 347–358, Aug. 2012, doi: 10.1016/j.rse.2012.04.002.

[17] A. L. Nguy-Robertson *et al.*, "Estimating green LAI in four crops: Potential of determining optimal spectral bands for a universal algorithm," *Agric. Forest Meteorol.*, vol. 192/193, pp. 140–148, Jul. 2014, doi: 10.1016/j.agrformet.2014.03.004.

[18] A. Viña, A. A. Gitelson, A. L. Nguy-Robertson, and Y. Peng, "Comparison of different vegetation indices for the remote assessment of green leaf area index of crops," *Remote Sens. Environ.*, vol. 115, no. 12, pp. 3468–3478, Dec. 2011, doi: 10.1016/j.rse.2011.08.010.

[19] A. Kross, H. McNairn, D. Lapen, M. Sunohara, and C. Champagne, "Assessment of rapideye vegetation indices for estimation of leaf area index and biomass in corn and soybean crops," *Int. J. Appl. Earth Obs. Geoinf.*, vol. 34, pp. 235–248, Feb. 2015, doi: 10.1016/j.jag.2014.08.002.

[20] D. Ganeva, E. Roumenina, G. Jelev, M. Banov, V. Krasteva, and V. Kolchakov, "Applicability of parametric and nonparametric regression models for retrieval of crop canopy parameters for winter rapeseed and wheat crops using Sentinel-2 multispectral data," in *Proc. 7th Int. Conf. Remote Sens. Geoinf. Environ.*, Jun. 2019, vol. 11174, Art. no. 111740J, doi: 10.1117/12.2533651.

[21] N. Ahmadian, T. Ullmann, J. Verrelst, E. Borg, R. Zölitz, and C. Conrad, "Biomass assessment of agricultural crops using multi-temporal dual-polarimetric TerraSAR-X data," *J. Photogramm. Remote Sens. Geoinf. Sci.*, vol. 87, no. 4, pp. 159–175, Oct. 2019, doi: 10.1007/s41064-019-00076-x.

[22] K. Harfenmeister, D. Spengler, and C. Weltzien, "Analyzing temporal and spatial characteristics of crop parameters using Sentinel-1 backscatter data," *Remote Sens,* vol. 11, no. 13, Jan. 2019, Art. no. 1569, doi: 10.3390/rs11131569.

[23] M. Vreugdenhil *et al.*, "Sensitivity of sentinel-1 backscatter to vegetation dynamics: An austrian case study," *Remote Sens.,* vol. 10, no. 9, Sep. 2018, Art. no. 1396, doi: 10.3390/rs10091396.

[24] G. Wiseman, H. McNairn, S. Homayouni, and J. Shang, "RADARSAT-2 polarimetric SAR response to crop biomass for agricultural production monitoring," *IEEE J. Sel. Topics Appl. Earth Obs. Remote Sens.*, vol. 7, no. 11, pp. 4461–4471, Nov. 2014.

[25] M. Ameline, R. Fieuzal, J. Betbeder, J. Berthoumieu, and F. Baup, "Estimation of corn yield by assimilating SAR and optical time series into a simplified agro-meteorological model: From diagnostic to forecast," *IEEE J. Sel. Topics Appl. Earth Obs. Remote Sens.*, vol. 11, no. 12, pp. 4747–4760, Dec. 2018.

[26] F. Baup, M. Ameline, R. Fieuzal, F. Frappart, S. Corgne, and J.-F. Berthoumieu, "Temporal evolution of corn mass production based on agro-meteorological modelling controlled by satellite optical and SAR images," *Remote Sens.*, vol. 11, no. 17, Jan. 2019, Art. no. 1978, doi: 10.3390/rs11171978.

[27] F. Baup, L. Villa, R. Fieuzal, and M. Ameline, "Sensitivity of X-band (σ0, γ) and optical (NDVI) satellite data to corn biophysical parameters," *Adv. Remote Sens.*, vol. 5, no. 2, pp. 103–117, May 2016, doi: 10.4236/ars.2016.52009.

[28] J. Betbeder, R. Fieuzal, Y. Philippets, L. Ferro-Famil, and F. Baup, "Contribution of multitemporal polarimetric synthetic aperture radar data for monitoring winter wheat and rapeseed crops," *J. Appl. Remote Sens.*, vol. 10, no. 2, May 2016, Art. no. 026020, doi: 10.1117/1.JRS.10.026020.

[29] R. Fieuzal, C. M. Sicre, and F. Baup, "Estimation of corn yield using multi-temporal optical and radar satellite data and artificial neural networks," *Int. J. Appl. Earth Obs. Geoinf.*, vol. 57, pp. 14–23, May 2017, doi: 10.1016/j.jag.2016.12.011.

[30] R. Fieuzal, F. Baup, and C. Marais-Sicre, "Monitoring wheat and rapeseed by using synchronous optical and radar satellite data—From temporal signatures to crop parameters estimation," *Adv. Remote Sens.*, vol. 2, no. 2, Jun. 2013, Art. no. 33222, doi: 10.4236/ars.2013.22020.

[31] M. Hosseini and H. McNairn, "Using multi-polarization C- and L-band synthetic aperture radar to estimate biomass and soil moisture of wheat fields," *Int. J. Appl. Earth Obs. Geoinf.*, vol. 58, pp. 50–64, Jun. 2017, doi: 10.1016/j.jag.2017.01.006.

[32] Y. Inoue *et al.*, "Season-long daily measurements of multifrequency (Ka, ku, x, c, and L) and full-polarization backscatter signatures over paddy rice field and their relationship with biological variables," *Remote Sens. Environ.*, vol. 81, no. 2, pp. 194–204, Aug. 2002, doi: 10.1016/S0034-4257(01)00343-1.

[33] A. Veloso *et al.*, "Understanding the temporal behavior of crops using Sentinel-1 and Sentinel-2-like data for agricultural applications," *Remote Sens. Environ.*, vol. 199, pp. 415–426, Sep. 2017, doi: 10.1016/j.rse.2017.07.015.

[34] A. Mercier, J. Betbeder, S. Rapinel, N. Jegou, J. Baudry, and L. Hubert-Moy, "Evaluation of Sentinel-1 and -2 time series for estimating LAI and biomass of wheat and rapeseed crop types," *J. Appl. Remote Sens.*, vol. 14, no. 2, May 2020, Art. no. 2, doi: 10.1117/1.JRS.14.024512.

[35] BBCH Monograph, *Growth Stages of Mono- and Dicotyledonous Plants*, Meier Uwe. Berlin/Braunschweig, Germany: Federal Biological Res. Centre for Agriculture and Forestry, 2001. [Online]. Available: https://www.openagrar.de/receive/openagrar_mods_00042351, Accessed: Dec. 14, 2020.

[36] V. Demarez, S. Duthoit, F. Baret, M. Weiss, and G. Dedieu, "Estimation of leaf area and clumping indexes of crops with hemispherical photographs," *Agric. Forest Meteorol.*, vol. 148, no. 4, pp. 644–655, Apr. 2008, doi: 10.1016/j.agrformet.2007.11.015.

[37] M. Weiss and F. Baret, "CAN_Eye V6.4.91 user manual," UMR1114 EMMAH, INRA, Avignon, France, 2017. [Online]. Available: https://www6.paca.inrae.fr/can-eye/content/download/3052/30819/version/4/file/CAN_EYE_User_Manual.pdf

[38] N. Gorelick, M. Hancher, M. Dixon, S. Ilyushchenko, D. Thau, and R. Moore, "Google earth engine: Planetary-scale geospatial analysis for everyone," *Remote Sens. Environ.*, vol. 202, pp. 18–27, Dec. 2017, doi: 10.1016/j.rse.2017.06.031.

[39] Y. Kim and J. van Zyl, "Vegetation effects on soil moisture estimation," in *Proc. IEEE Int. Geosci. Remote Sens. Symp.*, Sep. 2004, vol. 2, pp. 800–802, doi: 10.1109/IGARSS.2004.1368525.

[40] R. Nasirzadehdizaji, F. Balik Sanli, S. Abdikan, Z. Cakir, A. Sekertekin, and M. Ustuner, "Sensitivity analysis of multi-temporal sentinel-1 SAR parameters to crop height and canopy coverage," *Appl. Sci.*, vol. 9, no. 4, Jan. 2019, Art. no. 655, doi: 10.3390/app9040655.

[41] F. Baret, S. Jacquemoud, G. Guyot, and C. Leprieur, "Modeled analysis of the biophysical nature of spectral shifts and comparison with information content of broad bands," *Remote Sens. Environ.*, vol. 41, no. 2, pp. 133–142, Aug. 1992, doi: 10.1016/0034-4257(92)90073-S.

[42] S. Jacquemoud and F. Baret, "PROSPECT: A model of leaf optical properties spectra," *Remote Sens. Environ.*, vol. 34, no. 2, pp. 75–91, Nov. 1990, doi: 10.1016/0034-4257(90)90100-Z.

[43] W. Verhoef, "Earth observation modeling based on layer scattering matrices," *Remote Sens. Environ.*, vol. 17, no. 2, pp. 165–178, Apr. 1985, doi: 10.1016/0034-4257(85)90072-0.

[44] W. Verhoef, "Light scattering by leaf layers with application to canopy reflectance modeling: The SAIL model," *Remote Sens. Environ.*, vol. 16, no. 2, pp. 125–141, Oct. 1984, doi: 10.1016/0034-4257(84)90057-9.

[45] F. X. Kneizys, D. C. Robertson, L. W. Abreu, P. Acharya, G. P. Anderson, and L. S. Rothman, "The MODTRAN 2/3 report and LOWTRAN 7 MODEL," Philips Laboratory, Ontar Corporation, North Andover, MA, USA, Jan. 1996.

[46] H. Poilvé, "BioPar methods compendium MERIS FR biophysical products," Report g2-BP-RP-038, EC geoland2 Project FP-7-218795, Toulouse, France, 2010.
[47] A. Gorrab, M. Ameline, C. Albergel, and F. Baup, "Use of sentinel-1 multi-configuration and multi-temporal series for monitoring parameters of winter wheat," *Remote Sens.,* vol. 13, no. 4, Jan. 2021, Art. no. 553, doi: 10.3390/rs13040553.
[48] J.-F. Dejoux, S. Recous, J.-M. Meynard, I. Trinsoutrot, and P. Leterme, "The fate of nitrogen from winter-frozen rapeseed leaves: Mineralization, fluxes to the environment and uptake by rapeseed crop in spring," *Plant Soil*, vol. 218, no. 1, pp. 257–272, Jan. 2000, doi: 10.1023/A:1014934924819.
[49] B. Duchemin, P. Maisongrande, G. Boulet, and I. Benhadj, "A simple algorithm for yield estimates: Evaluation for semi-arid irrigated winter wheat monitored with green leaf area index," *Environ. Model. Softw.*, vol. 23, no. 7, pp. 876–892, Jul. 2008, doi: 10.1016/j.envsoft.2007.10.003.
[50] F. Baup, R. Fieuzal, and J. Betbeder, "Estimation of soybean yield from assimilated optical and radar data into a simplified agrometeorological model," in *Proc. IEEE Int. Geosci. Remote Sens. Symp.*, Jul. 2015, pp. 3961–3964.
[51] J. Betbeder, R. Fieuzal, and F. Baup, "Assimilation of LAI and dry biomass data from optical and SAR images into an agro-meteorological model to estimate soybean yield," *IEEE J. Sel. Topics Appl. Earth Obs. Remote Sens.*, vol. 9, no. 6, pp. 2540–2553, Jun. 2016.
[52] R. Fieuzal, C. M. Sicre, and F. Baup, "Estimation of sunflower yield using a simplified agrometeorological model controlled by optical and SAR satellite data," *IEEE J. Sel. Topics Appl. Earth Obs. Remote Sens.*, vol. 10, no. 12, pp. 5412–5422, Dec. 2017.
[53] H. Akaike, "Information theory and an extension of maximum likelihood principle," in *Proc. 2nd Int. Symp. Inf. Theory*, 1973, pp. 267–281.
[54] W. Zhang *et al.*, "Compact polarimetric response of rape (Brassica napus L.) at C-band: Analysis and growth parameters inversion," *Remote Sens.,* vol. 9, no. 6, Jun. 2017, Art. no. 591, doi: 10.3390/rs9060591.
[55] H. Yang *et al.*, "In-season biomass estimation of oilseed rape (Brassica napus L.) using fully polarimetric SAR imagery," *Precis. Agric.*, vol. 20, no. 3, pp. 630–648, Jun. 2019, doi: 10.1007/s11119-018-9587-0.

Aubin Allies was born in Ivry-sur-Seine, France, in 1992. He received the B.S. degree in ecology and biology of organisms, the M.S. degree in hydrology and environmental hazards, and the Ph.D. degree in geosciences on the estimation of evapotranspiration from remote sensing in West Africa, from the University of Montpellier, Montpellier, France, in 2013, 2015, and 2018, respectively, and the M.S. degree in ecology and biodiversity management engineering in 2020 from the University of Montpellier.

He is currently working with the Institut Europlace de Finance, Paris, Airbus Defence and Space Geo SA, Toulouse, and the CESBIO, Toulouse, on the estimation of production variations of field crops from remote sensing time series with a view to creating index-based crop insurance. His research interests include optical, thermal and microwave remote sensing applied to land surfaces to retrieve and monitor essential variables for different scientific fields, including water and energy budgets, ecology and biological conservation, and crops monitoring. He is also involved in assimilation exercises of satellite data into agrometeorological and land surface models.

Antoine Roumiguié was born in Toulouse, France, in 1987. He received M.S. degree engineer in agronomy from the Ecole d'Ingénieurs de Purpan, Toulouse, France, in 2010 and M.S. degree in land planning and remote sensing from the University Paul Sabatier, Toulouse, in 2012, de Purpan.

Since 2016, he has been an Agronomic Product Design Engineer working with Airbus Defence and Space Geo SA, Toulouse. He is directly involved in the development and the operation of agroinsurance programs that are currently running.

Jean-François Dejoux was born in Le Creusot, France, in 1970. He received the M.S. and Ph.D. degrees in agronomy from the French National School of Agronomy, Paris, France, in 1993 and 1999, respectively. His Ph.D. was dealing with the evaluation of early sowing of winter oilseed rape.

From 2000 to 2005, he was charged with research and development activities in conventional and organic farming with the Rhônes-Alpes Regional Chamber of Agriculture, Lyon, France. Since 2006, he has been working with the Centre d'Etudes Spatiales de la BIOsphère, Toulouse, France. His activities concern experimentations and fields measurements to calibrate and validate remote sensing missions and crop models.

Rémy Fieuzal received the M.S. degree in ecology, biostatistics, and modeling in 2007 and the Ph.D. degree in remote sensing and agronomy in 2013 for his work on the contributions of radar satellite data for the estimation of biophysical parameters of agricultural land from Paul Sabatier University, Toulouse, France.

He works on image processing and analysis of satellite data acquired in the optical and microwave domains with the Centre d'Etudes Spatiales de la BIOsphère, Toulouse. His research works focus on the mapping of different surface parameters (leaf area index, biomass, irrigation or soil moisture) and the modeling of agrosystems (crop yield estimates or water and carbon balance components).

Anne Jacquin was born in Toulouse, France, in 1978. She received the B.S. and M.S. degrees in agriculture from Purpan Engineer School, Toulouse, France, in 2001, the M.S. degree in remote sensing from the Pierre et Marie Curie University, Paris, France, in 2002, and the Ph.D. degree in ecosystems and agroecosystems functioning from Toulouse University, Toulouse, France, in 2010.

From 2002 to 2017, she was a University Lecturer and a Researcher in remote sensing and agromodeling applied to the management of agriculture and natural resources with the French National Institute of Agronomy (INRAe), Toulouse. Since 2017, she has been an Agriculture and Environment Solutions Developer with AIRBUS Defence and Space GEO Intelligence, Toulouse. Her research and development interests include new satellite-derived services and solutions in order to produce reliable information on the status of crops, forest, and other natural land covers and provide practical recommendations that meet the needs of different actors (from farmers to institutional authorities).

Dr. Jacquin was a recipient of the Leopold Escande Award for her Ph.D. delivered in 2010 by the National Polytechnic Institute, Toulouse.

Amanda Veloso received the B.S. degree in electrical engineering from the University of Brasilia, Brasília, Brazil, and the "Ecole Nationale Supérieure d'Electronique, Informatique et Télécommunications de Bordeaux," Talence, France, in 2008, the M.S. degree from the University of Bordeaux-I, Bordeaux, France, specializing in image and signal processing in 2010, and the Ph.D. degree in remote sensing applied to agriculture and ecology from Toulouse III Paul Sabatier University, Toulouse, France, in 2014.

Her thesis concerned the assessment of carbon and water continental cycles and budgets for crop ecosystems. From 2014 to 2016, she was a Postdoctoral Fellow with the Centre D'Etudes Spatiales de la Biosphère. She is currently working with AIRBUS DS GEO on the use of remote sensing data for precision agriculture applications. Her main research interests include the estimation of biophysical variables from multitemporal optical and radar remote sensing data as well as their application in crop modeling approaches.

Luc Champolivier received the M.S. degree in plant biology and physiology from the University of Orléans, Orléans, France, in 1983.

Since 1985, he has been working with Terres Inovia, the French agricultural research institute carrying out applied research on oilseed plants and protein crops. He is in charge of research and development activities in minerals and water supply for crops and in the design of decision support tools in crop management for farmers, using remote sensing and modeling.

Frédéric Baup received the M.S. degree in microwave and optical telecommunications and the Ph.D. degree in SAR remote sensing from the University Paul Sabatier, Toulouse, France, in 2003 and 2007, respectively.

Since 2008, he has been a Researcher in microwave remote sensing with the Centre d'Etudes Spatiales de la BIOsphère Laboratory, Auch, France. His research interests include microwave remote sensing applied to land surfaces and SAR image analysis to monitor spatio-temporal variations of soil (moisture and roughness) and vegetation (biomass) properties over agricultural or natural areas. His education interests are focused on physics and remote sensing sciences. He is involved in the development of the inversion method for the estimation of surface parameters (soil and vegetation) from multifrequency microwave data (*X*-, *C*-, and *L*-band), the combination of optical, thermal, and microwave satellite data to improve the land surface monitoring, and in the assimilation of satellite data into agrometeorological models.